RHODES UNIVERSITY

Where leaders learn

Calibration and Imaging with Variable Radio Sources

Author:

Ulrich Armel Mbou Sob

Supervisors:

Dr. Sandeep Sirothia &

Dr. Trienko Grobler &

Prof. Oleg Smirnov

A thesis submitted in fulfilment of the requirements for the degree of

Masters of Science

in the

Centre for Radio Astronomy Techniques and Technologies

Department of Physics and Electronics

March 2017

Abstract

Calibration of radio interferometric data is one of the most important steps that are required to produce high dynamic range radio maps with high fidelity. However, naive calibration (inaccurate knowledge of the sky and instruments) leads to the formation of calibration artefacts: the generation of spurious sources and the deformations in the structure of extended sources. A particular class of calibration artefacts, called ghost sources, which results from calibration with incomplete sky models has been extensively studied by Grobler *et al.* (2014, 2016) and Wijnholds *et al.* (2016). They developed a framework which can be used to predict the fluxes and positions of ghost sources. This work uses the approach initiated by these authors to study the calibration artefacts and ghost sources that are produced when variable sources are not considered in sky models during calibration. This work investigates both long-term and short-term variability and uses the root mean square (rms) and power spectrum as metrics to evaluate the "quality" of the residual visibilities obtained through calibration. We show that the overestimation and underestimation of source flux density during calibration produces similar but symmetrically opposite results. We show that calibration artefacts from sky model errors are not normally distributed. This prevents them from being removed by employing advanced techniques, such as stacking. The power spectrums measured from the residuals with a variable source was significantly higher than those from residuals without a variable source. This implies advanced calibration techniques and sky model completeness will be required for studies such as probing the Epoch of Reoinization, where we seek to detect faint signals below thermal noise.

Acknowledgements

"The essence of all beautiful art is gratitude." –Friedrich Nietzche

Writing this thesis and doing this work has been a long and tedious experience. I would like in this section to express my heartfelt gratitudes to few people without which this will never have been possible.

First and foremost I thank my supervisors, Prof. Oleg Smirnov who gave me the honour of working with him, for all the academic advice and the funding through the aid of the Nation Research Foundation, Dr. Sandeep Sirothia for all his experience shared with me and the motivational ideas for this project and last but not least Dr. Trienko Grobler for all his attention, advice and support during the most difficult moments of this research. I also want to thank Prof. Stefan Wijnholds for all his contributions during my visit at ASTRON and his useful review comments and suggestions for the thesis. I am very grateful to the referees for all their constructive comments which greatly improved the clarity of the thesis.

My office mates and colleagues, Ridhima for all her support, encouragements and review of the thesis, Marcel and Ermias for the warm welcome in South Africa and for their brotherly love, Lerato for all her suggestions when writing the thesis. Alex, Kela, Sphe, Theo, Liju, Sami, Diana and all the other RATT members for their friendship and for making Grahamstown a beautiful place, Ronel and Sindi for handling all the administrative issues.

All my family members for all their moral support and prayers. Sonia and Eliz, my South African sisters for never letting me go hungry and taking marvellous care of me.

Finally I give praise to the almighty God for all his blessings and for never letting me down...

Contents

List of Figures

To my family...

Chapter 1

Introduction

Astronomy is one of the oldest natural sciences whose origins dates back to early civilizations such as the Babylonians, Greeks, Indians, Egyptians and Chinese. In a nutshell, Astronomy is the study of celestial objects, i.e. the moon, sun, planets, galaxies and so forth. Until the early 1930s, astronomy was done mainly using optical telescopes (optical astronomy). These observe the visible part of the electromagnetic spectrum. Radio astronomy, which is the study of celestial objects through their radio emission began in the 1930s following Karl Jansky's detection of the first radio signals (Jansky, 1933; Kraus, 1966). Karl Jansky, who was a radio engineer at the Bell Telephone Laboratories, detected signals from the Milky Way while working on transoceanic radio telecommunication. Following Jansky's discovery, research in radio astronomy increased dramatically, especially after the Second World War, where most of the technologies for radio and radar systems developed for the purpose of the war were used for radio astronomy studies. The radio spectrum ranges from 3 Hz to 3000 GHz and its radiations are mostly of non thermal origins. Radio astronomy has a considerable advantage over optical astronomy in that, radio waves are not severely obstructed (reflected and refracted) by dust and water vapour in the atmosphere as is the case for light waves.

During its early days, radio astronomy research was done mainly using single dish telescopes, but the quest for higher resolution led to the discovery of a technique called radio interferometry.

1.1 Radio Interferometry

Radio interferometry is the principle of operating several radio telescopes as one in order to produce images with high resolution. An array of radio telescopes that operates in

such a way is called an interferometer. The resolution of an interferometer is defined as,

$$\theta \approx 1.22\frac{\lambda}{B},$$

where θ is the resolution of the interferometer, λ is the wavelength of the incoming signal measured in meters and B the maximum baseline i.e. the longest distance between each pair of telescopes measured in meters. This implies by making B as large as possible we get the same resolution as that of a single dish telescope with a diameter B. Figure 1.1 is a simple two element interferometer with the two antennas pointing at a distant source in a direction indicated by the unit vector $\vec{s}$.

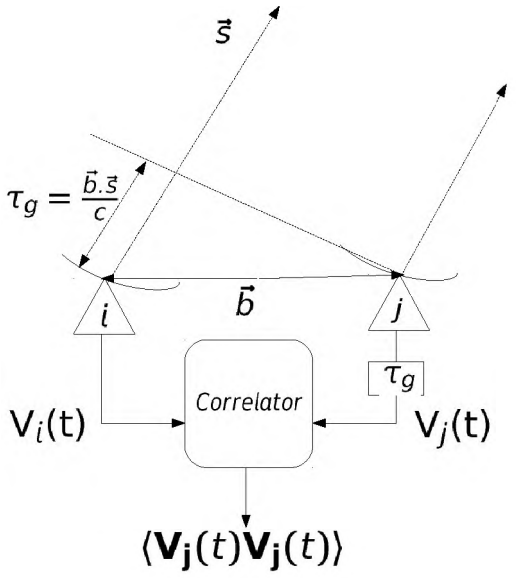

FIGURE 1.1: A schematic representation of a simple two element interferometer. The signal reaches antenna j before antenna i thus a delay is introduced in the signal from j before both signals are correlated to get the visibilities.

An interferometer measures the coherence of the signals from a pair of antenna. These measurements are called visibilities. From Figure 1.1, the signal from the source in the direction $\vec{s}$ reaches antenna j before antenna i. The delay between the two arrival times is called the geometric delay, τ_g and is defined as,

$$\tau_g = \frac{\vec{b}.\vec{s}}{c},$$

where $\vec{b}$ is the baseline vector between the antennas, $\vec{s}$ the signal direction vector and c is the speed of light. To account for time delay, the signals from antenna j are delayed by τ_g before correlating (multiplication and averaging) with those from antenna i to obtain the visibilities.

Using (u, v, w) to represent the baseline vectors with w pointing in the direction of the source where (u, v, w) are measured in wavelengths and (l, m) which are direction cosines measured with respect to the u, v axes, the measured visibilities are related to the sky brightness by the Van Cittert-Zernike theorem (Thompson *et al.*, 2008):

$$V(u,v,w) = \int_{-\infty}^{\infty}\int_{-\infty}^{\infty} A(l,m)I(l,m)e^{-2\pi i[ul+vm+w(\sqrt{1-l^2-m^2}-1)]}\frac{dldm}{\sqrt{1-l^2-m^2}} \quad (1.1)$$

where $V(u, v, w)$ represents the measured visibilities at the baseline coordinates (u, v, w), $I(l, m)$ represents the sky brightness distribution and $A(l, m)$ represents the effective collecting area of the antennas with respect to the direction of the incoming radiation.

Equation 1.1 is generally approximated to be a Fourier transform by eliminating the w phase term as follows

- If the observation is made with a coplanar array, then $w = 0$ and Equation 1.1 becomes

$$V(u,v,w) = \int_{-\infty}^{\infty}\int_{-\infty}^{\infty} A(l,m)I(l,m)e^{-2\pi i(ul+vm)}\frac{dldm}{\sqrt{1-l^2-m^2}} \quad (1.2)$$

  which is a two dimensional Fourier transform.

- If we are imaging a very small region in the sky then the term $\sqrt{1-l^2-m^2} \approx 1$ and Equation 1.1 becomes

$$V(u,v,w) = \int_{-\infty}^{\infty}\int_{-\infty}^{\infty} A(l,m)I(l,m)e^{-2\pi i(ul+vm)}dldm \quad (1.3)$$

  which is again a two dimensional Fourier transform.

The term $A(l, m)$ is most often assumed to be 1 for simplicity and the Van Cittert-Zernike theorem is stated as,

$$V(u,v) = \int_{-\infty}^{\infty}\int_{-\infty}^{\infty} I(l,m)e^{-2\pi i(ul+vm)}dldm \quad (1.4)$$

Thus the measured visibilities and the sky brightness are Fourier pairs and the sky brightness can readily be recovered from the measured visibilities by an inverse Fourier transform.

$$I(l,m) = \int_{-\infty}^{\infty}\int_{-\infty}^{\infty} V(u,v)e^{2\pi i(ul+vm)}dudv \quad (1.5)$$

1.2 Calibration and Imaging

In practice the picture is not as simple as stated in Equation 1.1, since the signals from the sources are corrupted by different factors as they travel to the antennas. The visibilities we measure are not a perfect representation of the sky, hence we need to correct these visibilities in a process called calibration, before imaging. Thus, calibration is the process of correcting for instrumental and ionospheric/tropospheric effects that corrupt the measured visibilities. Technically, calibration consists of using a sky model formed with our existing knowledge of the observed field to fit the measured data in a well defined mathematical framework such as the radio interferometer measurement equation (Hamaker *et al.*, 1996; Smirnov, 2011). Various calibration techniques exist and they are generally used all together to get the best calibration possible. These include calibration with calibrator sources, calibration with existing sky models and *self-calibration* or *selfcal* (Cornwell and Wilkinson, 1981). All of these will be discussed in detail in the next chapter.

Furthermore, we do not make continuous measurements of the visibilities, we sample the visibilities only at certain (u, v) points in the uv space. If we define our sampling function by $S(u, v)$ such that $S(u, v) = 1$ when ever a measurement is made and 0 otherwise, then our reconstructed sky image is defined as,

$$I_d(l, m) = \int_{-\infty}^{\infty}\int_{-\infty}^{\infty} S(u, v)V(u, v)e^{2\pi i(ul+vm)}dudv \tag{1.6}$$

$$= PSF * I_{true}(l, m) \tag{1.7}$$

where $I_d(l, m)$ is the reconstructed sky image, $I_{true}(l, m)$ is the true sky image, $*$ represents convolution, $PSF = \int_{-\infty}^{\infty}\int_{-\infty}^{\infty} S(u, v)e^{2\pi i(ul+vm)}dudv$ is called the Point Spread Function and represents the interferometer response to a 1 Jy point source. The reconstructed image is called the "dirty image" because it is a convolution of the true sky and the point spread function. During imaging this problem is solved in a process called "cleaning" or deconvolution (Högbom, 1974; Cornwell *et al.*, 1999).

1.3 Variable Sources

Variable sources (Kellermann and Pauliny-Toth, 1968) are sources whose flux density varies with time. The time scales for this variability may range from few seconds to years. Various surveys have been carried on different fields, to search for different variables, transient sources and to study the variability rates in these fields. Thyagarajan *et al.* (2011) presents results from a variability and transient search conducted using 55000 snapshot images of the FIRST survey. Thyagarajan *et al.* (2011) identified 1,627 variable and transient objects down to mJy, with variability rates of $\approx$ 20 %. A recent search is presented in Rowlinson *et al.* (2016) using data from the Murchison Widefield Array (MWA) on timescales of 28 s to 1 year. Rowlinson *et al.* (2016) did not identify any transient candidate but, obtained Fast Radio Burst(FRBs) rates (<82 FRBs per sky per day for dispersion measures <700 pc cm^{-3}) consistent with existing literatures. Mooley *et al.* (2016) gives variability rates for different classes of variable sources using data from the Caltech-NRAO Stripe 82 Survey (CNSS). Stewart *et al.* (2016) describes the result of a four-month campaign searching for lower frequency variable and transient sources near the North Celestial pole using the Low Frequency Array (LOFAR). Stewart *et al.* (2016) found no variable candidate, but found a convincing transient candidate. This transient had a flux density of 15-25 Jy at 60 MHz, with a duration of few minutes.

The advent of the new generation of radio telescopes such as, the Square Kilometre Array (SKA; Schilizzi *et al.*, 2008) provides a massive burst to the amount of sciences, and explorations which will be achievable for variable and transient sources. Fender *et al.* (2015) gives an overview of the different sciences for variables and transients which will be possible with SKA, and how SKA can be operated to maximise their outputs. Furthermore Fender *et al.* (2015) review results from few surveys and, also provides expected variable and transient rates for SKA. Fender *et al.* (2015) gives a potential of $\approx$ 600 variable sources deg^{-2} at SKA flux levels. This value is very high and emphasises the necessity of investigating source variability.

Variability in sources generally arise from different sorts of reasons. These include changes in sources observed luminosity and obstructions of the amount of radiations travelling from the sources to the earth for one reason or the other. Different types of radio sources exhibits variability. In the next section we present the blazar PKS 1510-089 which was recently observed using the Karoo Array telescope (KAT-7; Booth *et al.*, 2009). Other examples of variable sources include flare stars (Osten and Bastian, 2008) and binary systems such as GRS 1915+105 (Foster *et al.*, 1996).

1.3.1 PKS 1510-089

PKS 1510-089 is a flat spectrum blazar at a redshift of $z = 0.361$ with celestial coordinates $\alpha = 15^h12^m50.5^s$ and $\delta = -09^d06^m00^s$ (Barnacka *et al.*, 2014). The source PKS 1510-089 is well known for its long-term variability and has recently shown hints of having some intrinsic variability on short time scales (Kadota *et al.*, 2012). PKS 1510-089 was recently monitored with KAT-7 between October 2011 and October 2014 (Oozeer *et al.*, 2015). Figure 1.2 is an image of the field and a plot of its flux density during this period showing some significant long-term variations. It was measured to have a modulation of index (MI) of $\approx 16\%$ and a strong amplitude variability (V_{rms}) of $\approx 46\%$(Oozeer *et al.*, 2015). The MI and V_{rms} were defined respectively as

$$MI = 100 \times \frac{2\sigma}{\langle S \rangle} \tag{1.8}$$

$$V_{rms} = \frac{100}{\langle S \rangle} \sqrt{\frac{\sum [S_i - \langle S \rangle]^2 - \sum \delta S_i^2}{N}}, \tag{1.9}$$

where S is the sequence of the measured flux values, $\langle S \rangle$ is the mean of the measured flux values, σ is the standard deviation of the measured flux values and N is the total number of observations. This observation provided an important motivation for this thesis.

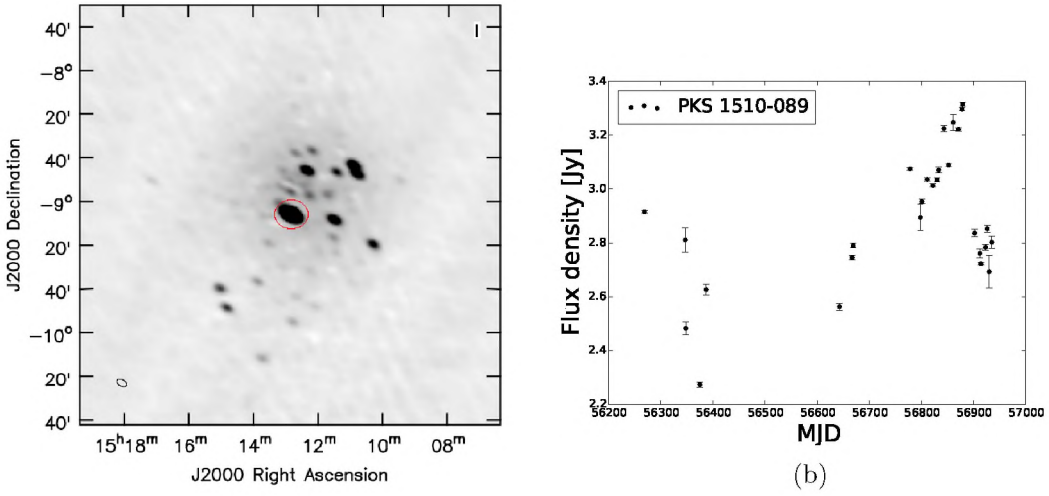

(a) (b)

FIGURE 1.2: Left: An image of the PKS 1510-089 field observed at 1.8 GHZ by Nadeem Oozeer with KAT-7, PKS 1510-089 is the point source in the red ellipse. Right: Light curve of PKS 1510-089 between November 2012 and October 2014. The dates are in modified julian dates. This source was measured to have a mean of 2.8 Jy, standard deviation of 0.25 Jy.

1.4 Thesis Motivation

MeerKAT and the future Square Kilometer Array (SKA) are expected to reach unprecedented sensitivity levels and data rates. Calibration of these new instruments will be very important if these instruments are to achieve their science goals. It is well known that calibration errors lead to calibration artefacts which reduce the fidelity and science output of radio maps.

A particular class of calibration artefacts called ghost-sources have been shown to result from calibration with incomplete sky models (Grobler *et al.*, 2014; Wijnholds *et al.*, 2016; Grobler *et al.*, 2016). These sources are usually very faint, but with the intended sensitivity and noise level of MeerKAT and SKA, these artefacts may become apparent. Future deep surveys such as MeerKAT International GHz Tiered Extragalactic Exploration (MIGHTEE), and the Evolutionary Map of the Universe (EMU), with the Australian Square Kilometer Array Pathfinder (ASKAP), which are aiming to detect very faint sources, will need to completely eliminate such artefacts during calibration.

Variable sources are not yet routinely considered in calibration pipelines and therefore will be a source of spurious artefacts. Variability of sources implies we will never get our sky models correct. The flux density of variable sources will always either be underestimated or overestimated. In this work we study how ignoring variability affects calibration. We do this by looking at the rms and the power spectrum of residual visibilities. The study demonstrates how inaccurate modelling of a single source introduces very bright artefacts in our residual visibilities.

The work presented here is more focused on long-term variability than short-term variability. For the sake of completeness we briefly touch on short-term variability. KAT-7 which is an engineering prototype for MeerKAT, is exclusively used for all the simulations. This is also to be consistent with Wijnholds *et al.* (2016) and KAT-7 monitoring of the variable blazar PKS 1510-089 which was one of our first motivations for this study.

1.5 Thesis Outline

The rest of the thesis consist of five chapters, whose content is summarised as follows:

- Chapter 2: This chapter presents a brief description of radio interferometry calibration. Here we demonstrate how calibration can be formulated as an optimization problem using the radio interferometry measurement equation. We present two calibration algorithms and recent developments in the field of calibration. We end this chapter by introducing calibration artefacts and reviewing Grobler *et al.* (2014) and Wijnholds *et al.* (2016).

- Chapter 3: In this chapter we investigate the effects of long-term variable sources on the rms of residual visibilities. The simulations here are done using the MeqTrees software package (Noordam and Smirnov, 2010).

- Chapter 4: This chapter provides an extension to the analysis of the results from Chapter 3. Here we develop a power spectrum estimator and apply it to the residuals obtained in Chapter 3.

- Chapter 5: This chapter extends the work from Chapter 3 by investigating the effects of short-term variability on the rms of residual visibilities.

- Chapter 6: This chapter presents the general conclusions from this work and suggests future research avenues.

Chapter 2

Calibration

In the field of radio astronomy, calibration is the process of solving and correcting for the systematic errors in interferometric data (Section 1.1). Examples of such corruptions are antenna gains, beam errors, antenna pointing errors and atmospheric effects. These aforementioned effects can be further classified into Direction Independent Effects (DIEs) and Direction Dependent Effects (DDEs). DIEs are propagation effects which are constant across the sky and thus are the same for all the sources and antennas. A common example of DIEs are the antenna gains. DDEs are propagation effects which are position dependent and thus vary for each source in the sky. Such errors include primary beam effects and ionospheric effects and they are in principle more complicated to solve for. Calibration is preceded by a process called *flagging* (Offringa *et al.*, 2012) during which severely corrupted data are removed. These include data corrupted by radio frequency interference (RFI), data from bad baselines and antenna failures during certain parts of the observation. We begin this chapter by presenting the radio interferometry measurement equation (RIME) which is a mathematical formalism used to model the propagation errors introduced into the visibilities during calibration, next we discuss two calibration algorithms and we conclude with calibration artefacts which are systematics produced during calibration.

2.1 Measurement Equation

Methodologically, calibration consists of finding gains which minimises the difference between the measured visibilities and predicted visibilities. The predicted visibility models all the propagation effects using an equation called the Radio Interferometry Measurement Equation (RIME) or simply the measurement equation (Hamaker *et al.*, 1996; Smirnov, 2011). In this section we present a simple mathematical derivation of

the RIME.

Suppose we have a sky consisting of a single point source emitting a quasi-monochromatic signal, in an xyz coordinate system with the z-axis along the direction of propagation. The signal may be represented by

$$\boldsymbol{e} = \begin{pmatrix} e_x \\ e_y \end{pmatrix}.$$

When this signal reaches the antenna it is converted into complex voltages by the antenna feeds. Antennas usually have two feeds which are orthogonal to each other (for example two linear dipoles or left/right circular feeds). Similarly to the input signal, the output voltage may be represented by a complex vector, $\boldsymbol{v}$ defined as

$$\boldsymbol{v} = \boldsymbol{J}\boldsymbol{e} \tag{2.1}$$

where $\boldsymbol{J}$ is a 2×2 matrix called the Jones matrix. The Jones matrix represents the cumulative product of all the propagation effects along the signal path.
A two-element interferometer as introduced in Section 1.1 measures the correlations of the output voltages from two antennas known as visibilities. For any two antennas p and q with respective output voltages $\boldsymbol{v}_p$ and $\boldsymbol{v}_q$

$$\boldsymbol{v}_p = \boldsymbol{J}_p\boldsymbol{e} \tag{2.2}$$
$$\boldsymbol{v}_q = \boldsymbol{J}_q\boldsymbol{e} \tag{2.3}$$

the visibility matrix is defined as

$$\begin{aligned} \boldsymbol{V}_{pq} &= 2\langle \boldsymbol{v}_p \boldsymbol{v}_q^H \rangle && (2.4)\\ &= 2\left\langle \begin{pmatrix} v_{px} \\ v_{py} \end{pmatrix} \begin{pmatrix} v_{qx}^* & v_{qy}^* \end{pmatrix} \right\rangle && (2.5)\\ &= 2\left\langle \begin{pmatrix} v_{px}v_{qx}^* & v_{px}v_{qy}^* \\ v_{py}v_{qx}^* & v_{py}v_{qy}^* \end{pmatrix} \right\rangle && (2.6) \end{aligned}$$

where $\langle . \rangle$ represents the expectation value, $(.)^H$ represents the conjugate transpose and $(.)^*$ represents the complex conjugate. Using the definition of $\boldsymbol{v}$ from Equation 2.1, we can rewrite the visibility matrix, $\boldsymbol{V}_{pq}$ as

$$\boldsymbol{V}_{pq} = 2\left\langle \begin{pmatrix} \boldsymbol{J}_p e_x e_x^* \boldsymbol{J}_q^H & \boldsymbol{J}_p e_x e_y^* \boldsymbol{J}_q^H \\ \boldsymbol{J}_p e_y e_x^* \boldsymbol{J}_q^H & \boldsymbol{J}_p e_y e_y^* \boldsymbol{J}_q^H \end{pmatrix} \right\rangle \tag{2.7}$$

Assuming that $\boldsymbol{J}_p$ and $\boldsymbol{J}_q$ are constant over the averaging interval they can be factorised as follows

$$\boldsymbol{V}_{pq} = \boldsymbol{J}_p \begin{pmatrix} 2\langle e_x e_x^* \rangle & 2\langle e_x e_y^* \rangle \\ 2\langle e_y e_x^* \rangle & 2\langle e_y e_y^* \rangle \end{pmatrix} \boldsymbol{J}_q^H \tag{2.8}$$

The bracket terms in Equation 2.8 are related to the Stokes parameters (I, Q, U, V), and the sky brightness $\mathcal{B}$, as follows (Born and Wolf, 1964; Hamaker *et al.*, 1996; Thompson *et al.*, 2008)

$$\begin{pmatrix} 2\langle e_x e_x^* \rangle & 2\langle e_x e_y^* \rangle \\ 2\langle e_y e_x^* \rangle & 2\langle e_y e_y^* \rangle \end{pmatrix} = \begin{pmatrix} I+Q & U+iV \\ U-iV & I-Q \end{pmatrix} = \mathcal{B} \tag{2.9}$$

Hence the RIME for a single point source may be written as

$$\boldsymbol{V}_{pq} = \boldsymbol{J}_p \mathcal{B} \boldsymbol{J}_q^H \tag{2.10}$$

The Jones matrix may be expanded to include all the propagation effects and the RIME for a single point source becomes

$$\boldsymbol{V}_{pq} = \boldsymbol{J}_{pm}(...(\boldsymbol{J}_{p2}(\boldsymbol{J}_{p1}\mathcal{B}\boldsymbol{J}_{q1}^H)\boldsymbol{J}_{q2}^H)...)\boldsymbol{J}_{qn}^H \tag{2.11}$$

Equation 2.11 is sometimes called the onion form of the RIME and note that m may be different from n, thus the number of propagation effects may not always be the same in each direction or antenna. Since matrix multiplication is not in general commutative, we need to preserve the order of the matrices which represents the order of occurrence of the different propagation effects. The equation may be restated for N sources as the following summation

$$\boldsymbol{V}_{pq} = \sum_s \boldsymbol{J}_{sp} \mathcal{B}_s \boldsymbol{J}_{sq}^H \tag{2.12}$$

where $\boldsymbol{J}_{sp}$ represents the propagation effects encountered by the signal from the source s on its path to the antenna p. The phase term introduced in Section 1.1 is denoted by $\boldsymbol{K}_p$ and is defined as $\boldsymbol{K}_p = e^{-2\pi i(u_p l + v_p m + w_p(n-1))}$. The antenna direction independent gains are denoted by $\boldsymbol{G}_p$ and the direction dependent primary beam is denoted by $\boldsymbol{E}_p$. Hence the RIME can explicitly be written as

$$\boldsymbol{V}_{pq} = \boldsymbol{G}_p \sum_s (\boldsymbol{E}_{sp}\boldsymbol{K}_{sp}\mathcal{B}_s\boldsymbol{K}_{sq}^H\boldsymbol{E}_{sq}^H)\boldsymbol{G}_q^H \tag{2.13}$$

Note that the gains, $\boldsymbol{G}$ can be removed out of the summation since they are DIE.
In reality the sky does not consist only of discrete point sources. Instead the sky has a continuous brightness distribution, $\mathcal{B}(\boldsymbol{\sigma})$ and in order to get the total visibility measured

by an interferometer we change the summation in Equation 2.13 to an integral over all the possible directions (i.e. over a unit sphere). This leads to the following equation

$$\boldsymbol{V}_{pq} = \boldsymbol{G}_p(\int_l \int_m \frac{1}{n} \boldsymbol{E}_p \mathcal{B} \boldsymbol{E}_q^H e^{-2\pi i(u_{pq}l + v_{pq}m + w_{pq}(n-1))} dldm) \boldsymbol{G}_q^H \tag{2.14}$$

The presence of the term $W_{pq} = \frac{1}{n} e^{-2\pi i(w_{pq}(n-1))}$ prevents us from treating Equation 2.14 as a 2D Fourier transform. Since $w_{pq} = w_p - w_q$, we can decompose W_{pq} into $W_{pq} = W_p W_q$ where $W_p = \frac{1}{\sqrt{n}} e^{-2\pi i(w_p(n-1))}$. Using this decomposition we define a new Jones term $\tilde{\boldsymbol{E}}_p = \boldsymbol{E}_p W_p$. Using these new terms Equation 2.14 can be rewritten as

$$\boldsymbol{V}_{pq} = \boldsymbol{G}_p(\int_l \int_m \tilde{\boldsymbol{E}}_p \mathcal{B} \tilde{\boldsymbol{E}}_q^H e^{-2\pi i(u_{pq}l + v_{pq}m)} dldm) \boldsymbol{G}_q^H \tag{2.15}$$

Furthermore we can define a new term for the brightness distribution, $\mathcal{B}$ as $\mathcal{B}_{pq} = \tilde{\boldsymbol{E}}_p \mathcal{B} \tilde{\boldsymbol{E}}_q^H$. $\mathcal{B}_{pq}$ represents the sky brightness distribution as seen by the interferometer baseline pq. Using this latter definition Equation 2.14 effectively becomes a Fourier transform.

$$\boldsymbol{V}_{pq} = \boldsymbol{G}_p(\int_l \int_m \mathcal{B}_{pq} e^{-2\pi i(u_{pq}l + v_{pq}m)} dldm) \boldsymbol{G}_q^H \tag{2.16}$$

Equation 2.16 is generally known as the full-sky RIME and it is simply the Van Cittert-Zernike theorem (Thompson *et al.*, 2008) stated in Section 1.1 the only difference being that it now includes the propagation effects.

Hence in practice, calibration is an optimization problem, where we use the measured visibilities and the model, or, predicted visibilities obtained from the RIME to compute the propagation effects. In practice the measured visibilities contain instrumental noise, so we write our final form of the RIME as

$$\boldsymbol{V}_{pq} = \boldsymbol{G}_p(\int_l \int_m \mathcal{B}_{pq} e^{-2\pi i(u_{pq}l + v_{pq}m)} dldm) \boldsymbol{G}_q^H + \boldsymbol{N}_{pq} \tag{2.17}$$

where $\boldsymbol{N}_{pq}$ is a 2×2 matrix representing the noise contribution. The noise matrix has complex Gaussian entries with mean zero and equal variance in the real and imaginary parts.

2.2 Calibration Algorithms

In Section 2.1 we derived the measurement equation and showed that calibration is in fact just an optimization problem. Various optimization algorithms exist and can be used for calibration. In the next two sections we focus on two calibration algorithms, the Levenberg-Marquardt (LM) (Levenberg, 1944; Marquardt, 1963) and the Stastiscal

efficient and Fast Calibration (StEFCal) (Mitchell *et al.*, 2008; Salvini and Wijnholds, 2014) algorithm. These two algorithms use two different approaches. LM splits the complex visibilities and gains into real and imaginary parts before solving for the gains whereas StEFCal solves for the gains directly as complex numbers (Smirnov and Tasse, 2015). Other calibration algorithms include: alternating least squares (ALS) (Boonstra and Van Der Veen, 2001) where we alternate between solving for the noise and solving for the gains, calibration using the expectation maximization algorithm (Kazemi *et al.*, 2011), robust calibration by Kazemi and Yatawatta (2013) where the noise is modelled with a t-distribution in order to account for the unmodelled sources and non linear optimization on a Riemannian Manifold (Yatawatta, 2013).

2.2.1 Levenberg-Marquardt (LM)

We saw in Section 2.1 that we could represent the visibilities from two antenna pairs p and q as

$$\boldsymbol{V}_{pq} = \sum_{i=1}^{K} \boldsymbol{J}_{pi}\mathcal{B}_{pqi}\boldsymbol{J}_{qi}^{H} + \boldsymbol{N}_{pq} \tag{2.18}$$

where K is the number of celestial sources, $\boldsymbol{V}_{pq}$ is a 2×2 matrix of complex numbers representing the measured visibilities, $\mathcal{B}_{pqi}$ is a 2×2 complex matrix representing the brightness of the source i and $\boldsymbol{J}$ is the Jones matrix (2×2 complex matrix representing the propagation effects). For an interferometer with N antennas, we have $\frac{N(N-1)}{2}$ independent pairs of antennas with visibilities defined as in Equation 2.18. Observations are generally averaged within short time intervals τ, during which the components of Equation 2.18 are assumed to be constant. We formulate our optimization problem by rewriting Equation 2.18 in vector form as described in Yatawatta *et al.* (2012)

$$\mathbf{vec}(\boldsymbol{V}_{pq}) = \sum_{i=1}^{K} \mathbf{vec}(\boldsymbol{J}_{pi}\mathcal{B}_{pqi}\boldsymbol{J}_{qi}^{H}) + \mathbf{vec}(\boldsymbol{N}_{pq}) \tag{2.19}$$

$$\mathbf{vec}(\boldsymbol{V}_{pq}) = \sum_{i=1}^{K} \boldsymbol{J}_{qi}^{*} \otimes \boldsymbol{J}_{pi}\mathbf{vec}(\mathcal{B}_{pqi}) + \mathbf{vec}(\boldsymbol{N}_{pq}) \tag{2.20}$$

$$\boldsymbol{u}_{pq} = \sum_{i=1}^{K} \boldsymbol{s}_{pqi} + \boldsymbol{n}_{pq} \tag{2.21}$$

where $\boldsymbol{s}_{pqi} = \boldsymbol{J}_{qi}^{*} \otimes \boldsymbol{J}_{pi}\mathbf{vec}(\mathcal{B}_{pqi})$, $\boldsymbol{u_{pq}} = \mathbf{vec}(\boldsymbol{V}_{pq})$ $\boldsymbol{n}_{pq} = \mathbf{vec}(\boldsymbol{N}_{pq})$, $\otimes$ denotes the Kronecker product, $\mathbf{vec}(.)$ is the vectorization operation used to transform a matrix to a column vector, $(.)^{T}$ represents the matrix transpose, $(.)^{H}$ represents the conjugate transpose. Equation 2.19 is transformed to Equation 2.20 using the following vectorization property: for three matrices $\boldsymbol{A}$, $\boldsymbol{B}$, $\boldsymbol{C}$ of appropriate sizes, $\mathbf{vec}(\boldsymbol{ABC}) = (\boldsymbol{C}^{T} \otimes \boldsymbol{A})\mathbf{vec}(\boldsymbol{B})$.

Since our optimization parameters, $\boldsymbol{J}$, are complex numbers we split them into real and imaginary parts

$$\Theta = [\mathrm{Re}(\boldsymbol{J}_{11}), \mathrm{Im}(\boldsymbol{J}_{11}), ...] \tag{2.22}$$

Similarly we split our visibilities matrices into real and imaginary parts as follows

$$\boldsymbol{s}_i(\Theta) = [\mathrm{Re}(\boldsymbol{s}^T_{12i}), \mathrm{Im}(\boldsymbol{s}^T_{12i}), \mathrm{Re}(\boldsymbol{s}^T_{13i}), ...]^T \tag{2.23}$$

$$\boldsymbol{y} = [\mathrm{Re}(\boldsymbol{v}^T_{12}), \mathrm{Im}(\boldsymbol{v}^T_{12}), \mathrm{Re}(\boldsymbol{v}^T_{13}), ...]^T \tag{2.24}$$

Given N antennas, K sources and sampling interval, τ we have N×K×4×2=N×K×8 optimization parameters and $\frac{N(N-1)}{2}$ $\times 8 \times \tau$ equations. Hence we have more equations than unknowns and the problem can effectively be solved. LM (Levenberg, 1944; Marquardt, 1963) algorithm is a damped modification of the Gauss-Newton (GN) algorithm. We define our cost function, $F(\Theta)$ as follows

$$F(\Theta) = \|\boldsymbol{y} - \sum_i^k \boldsymbol{s}_i(\Theta)\|^2 \tag{2.25}$$

$$= \|f(\Theta)\|^2 \tag{2.26}$$

where $f(\Theta) = \boldsymbol{y} - \sum_i^k \boldsymbol{s}_i(\Theta)$. The LM algorithm computes the size of the update, $\mathbf{h}$ at each step by modifying the GN algorithm to include a damping factor as follows (Madsen *et al.*, 2004)

$$GN; \quad (\mathcal{J}^T\mathcal{J})\mathbf{h} = -\mathcal{J}^T f(\Theta) \tag{2.27}$$

$$LM; \quad (\mathcal{J}^T\mathcal{J} + \mu\boldsymbol{H})\mathbf{h} = -\mathcal{J}^T f(\Theta) \tag{2.28}$$

where $\mathcal{J}_{ij} = \frac{\partial f_i(\Theta)}{\partial \Theta_j}$ is the Jacobain matrix, μ is the damping factor and $\boldsymbol{H}$ is the diagonal matrix of $\mathcal{J}^T\mathcal{J}$. Hence for LM the update h is given by

$$\mathbf{h} = -(\mathcal{J}^T\mathcal{J} + \mu\boldsymbol{H})^{-1}\mathcal{J}^T f(\Theta) \tag{2.29}$$

Thus, starting from some initial value, Θ_0, the estimate Θ^{k+1} at the $(k+1)^{th}$ iteration is defined as

$$\Theta^{k+1} = \Theta^k - \alpha(\mathcal{J}^T\mathcal{J} + \mu\boldsymbol{H})^{-1}\mathcal{J}^T f(\Theta) \tag{2.30}$$

where α is the rate parameter used to control the size of each update value.

2.2.2 Calibration as a Complex Optimization Problem and StEFCal

The traditional approach to optimizing a function of n complex variables $f(\boldsymbol{z})$, $\boldsymbol{z} = \boldsymbol{x} + i\boldsymbol{y}$, $\boldsymbol{z} \in \mathbb{C}^n$ is to treat the real and imaginary parts independently, turning f into a function of $2n$ real variables as we did in the discussion of the LM algorithm in Section 2.2.1. The LM algorithm relies on the inversion of the matrix $(\mathcal{J}^T\mathcal{J} + \mu\boldsymbol{H})$ whose dimensions correspond to the number of free parameters. This matrix may be very large and the cost of its inversion may be huge. In this section we present an alternative approach proposed by Amin *et al.* (2011) and Sorber *et al.* (2012) based on Wirtinger calculus. Following this approach we optimize $f(\boldsymbol{z}, \bar{\boldsymbol{z}})$ instead of $f(\boldsymbol{x}, \boldsymbol{y})$ using the Wirtinger derivatives where $\bar{\boldsymbol{z}}$ is the conjugate of $\boldsymbol{z}$:

$$\frac{\partial}{\partial \boldsymbol{z}} = \frac{1}{2}\left(\frac{\partial}{\partial \boldsymbol{x}} - i\frac{\partial}{\partial \boldsymbol{y}}\right), \tag{2.31}$$

$$\frac{\partial}{\partial \bar{\boldsymbol{z}}} = \frac{1}{2}\left(\frac{\partial}{\partial \boldsymbol{x}} + i\frac{\partial}{\partial \boldsymbol{y}}\right). \tag{2.32}$$

Using Equation 2.31 and 2.32 we modify the cost function Equation 2.26 from Section 2.2.1 to solve for complex gain as follows

$$F(\boldsymbol{z}, \bar{\boldsymbol{z}}) = \|\boldsymbol{y} - \sum_i^k \boldsymbol{s}_i(\boldsymbol{z}, \bar{\boldsymbol{z}})\|^2 \tag{2.33}$$

$$= \|f(\boldsymbol{z}, \bar{\boldsymbol{z}})\|^2 \tag{2.34}$$

Let us treat $\boldsymbol{z}$ and $\bar{\boldsymbol{z}}$ as independent variables, we define a parameter vector containing both as

$$\tilde{\boldsymbol{z}} = \begin{bmatrix} \boldsymbol{z} \\ \bar{\boldsymbol{z}} \end{bmatrix}$$

Then we define

$$\mathcal{J} = \frac{\partial f(\boldsymbol{z}, \bar{\boldsymbol{z}})}{\partial \boldsymbol{z}}, \quad \bar{\mathcal{J}} = \frac{\partial f(\boldsymbol{z}, \bar{\boldsymbol{z}})}{\partial \bar{\boldsymbol{z}}} \quad \textit{and} \quad \tilde{f}(\boldsymbol{z}, \bar{\boldsymbol{z}}) = \begin{bmatrix} f(\boldsymbol{z}) \\ f(\bar{\boldsymbol{z}}) \end{bmatrix}$$

where $\mathcal{J}$ and $\bar{\mathcal{J}}$ are the partial and partial conjugate Jacobian. The full complex Jacobian $\tilde{J}$ is then written in block matrix form as

$$\tilde{J} = \begin{bmatrix} \mathcal{J} & \bar{\mathcal{J}} \\ \bar{\mathcal{J}}^* & \mathcal{J}^* \end{bmatrix}$$

where $(.)^*$ represents element by element conjugation.

Similarly as in Section 2.2.1 the size of the update at each step for the Gauss-Newton

(GN) and Levenberg-Marquardt (LM) algorithms are defined respectively as follows

$$GN; \quad \tilde{\partial \boldsymbol{z}} = \begin{bmatrix} \partial \boldsymbol{z} \\ \bar{\partial \boldsymbol{z}} \end{bmatrix} = -(\tilde{J}^H \tilde{J})^{-1} \tilde{J}^H f(\boldsymbol{z}, \bar{\boldsymbol{z}}) \tag{2.35}$$

$$LM; \quad \tilde{\partial \boldsymbol{z}} = \begin{bmatrix} \partial \boldsymbol{z} \\ \bar{\partial \boldsymbol{z}} \end{bmatrix} = -(\tilde{J}^H \tilde{J} + \mu \tilde{H})^{-1} \tilde{J}^H f(\boldsymbol{z}, \bar{\boldsymbol{z}}) \tag{2.36}$$

Smirnov and Tasse (2015) showed that for radio interferometry calibration the matrix $\tilde{J}^H \tilde{J}$ is very sparse. The sparsity of this matrix allows us to use various approximations for it. Smirnov and Tasse (2015) showed that the matrix $\tilde{J}^H \tilde{J}$ was diagonally dominant and could readily be approximated using a diagonal matrix. This reduces its cost of inversion from $O(N^3)$ to $O(N)$. Using this approach on the GN method for direction independent calibration, Smirnov and Tasse (2015) rederived StEFCal (Mitchell *et al.*, 2008; Salvini and Wijnholds, 2014).

StEFCal is an alternating direction implicit method for solving direction independent gains. Here the optimization problem is formulated as follows for non polarised sources

$$\boldsymbol{g} = \underset{\boldsymbol{g}}{\operatorname{argmin}} \|\boldsymbol{R} - \boldsymbol{G}\boldsymbol{M}\boldsymbol{G}^H\|^2 \tag{2.37}$$

where $\boldsymbol{R}$ is an $N \times N$ matrix representing the observed or measured visibilities, $\boldsymbol{M}$ is an $N \times N$ matrix representing the model or predicted visibilities, $\boldsymbol{G}$ is the $N \times N$ matrix of antenna gains, $\boldsymbol{g}$ is the diagonal of $\boldsymbol{G}$ and $\|.\|$ denotes the Frobenius norm.

Using StEFCal we solve for $\boldsymbol{G}^H$ holding $\boldsymbol{G}$ constant, then for $\boldsymbol{G}$ holding $\boldsymbol{G}^H$. Since $\Delta = \|\boldsymbol{R} - \boldsymbol{G}\boldsymbol{M}\boldsymbol{G}^H\|$ is hermitian, the two steps are identical and each iteration consists of only one step. Thus

$$\boldsymbol{G}^{[i]} = \underset{\boldsymbol{G}}{\operatorname{argmin}} \|\boldsymbol{R} - \boldsymbol{G}^{[i-1]}\boldsymbol{M}\boldsymbol{G}^H\|^2 \tag{2.38}$$

if we let $\boldsymbol{Z}^{[i]} = \boldsymbol{G}^{[i]}\boldsymbol{M}$

then $\Delta = \|\boldsymbol{R} - \boldsymbol{Z}\boldsymbol{G}^H\| \quad = \quad \sqrt{\|\sum_{i=1}^{p} \boldsymbol{R}_{:,p} - \boldsymbol{Z}_{:,p}\boldsymbol{g}_p^*\|}$

where $\boldsymbol{A}_{:,p}$ denotes the p^{th} column of the matrix $\boldsymbol{A}$.

Using the normal equation method the gains at the i^{th} iteration are readily given by

$$\boldsymbol{g}_p^{[i]} = \left\{ \frac{(\boldsymbol{Z}_{:,p}^{[i-1]})^H . \boldsymbol{R}_{:,p}}{(\boldsymbol{Z}_{:,p}^{[i-1]})^H . \boldsymbol{Z}_{:,p}^{[i-1]}} \right\}^* \tag{2.39}$$

where $*$ represents element wise conjugation.

The StEFCal algorithm provides a considerable computational advantage over most

calibration algorithms such as the Levenberg-Marquardt and Gauss-Newton algorithms which scale as P^3 where P is the number of free parameters.

2.3 Calibration Development

Over the years various calibration techniques have been developed to overcome various challenges that emerged due to the complexities in the design of new radio instruments. These techniques may broadly be classified into three categories namely First, Second and Third generation calibration (Noordam and Smirnov, 2010). In the following subsections we briefly discuss these categories and the reasons for their development.

2.3.1 First Generation Calibration (1GC)

This is generally the first step in any data reduction process, and was the main calibration procedure before 1980 (Noordam and Smirnov, 2010). The following are the calibration errors addressed during 1GC:

- Absolute flux density calibration during which the fluxes of the sources are scaled by a certain factor to their true fluxes.
- Bandpass calibration used to correct for the gain variations along frequency.
- Delay calibration used to correct for the phase delay errors.
- Gain calibration used to solve for the complex antenna gains.

Here we use sources with known fluxes and positions called calibrator sources to compute the gains. The gains are then applied to the target field. This is achieved by performing intermittent observations of the target and calibrator fields. In practice one or several calibrator sources may be used to address the various 1GC calibration errors. These calibrator sources are generally required to have the following properties (Thompson *et al.*, 2008):

- The absolute flux density calibrator should be bright so that a good signal to noise ratio is obtained in a short time. This minimizes the amount of time spent observing the calibrator source and maximises the time spent observing the target source.
- The calibrator source should preferably be unresolved so the precise details of its structure is not required.

- The calibrator source should be close enough to the target source for both of them to have the same atmospheric distortions.
- The bandpass calibrator should be a bright source with a flat spectrum.

2.3.2 Second Generation Calibration (2GC)

The era of second generation calibration (2GC) began in the eighties after the invention of self-calibration (selfcal) (Cornwell and Wilkinson, 1981). Self-calibration refers to an iterative calibration framework where the observed field is used to calibrate itself. Selfcal can be briefly described using the flowchart in Figure 2.1.

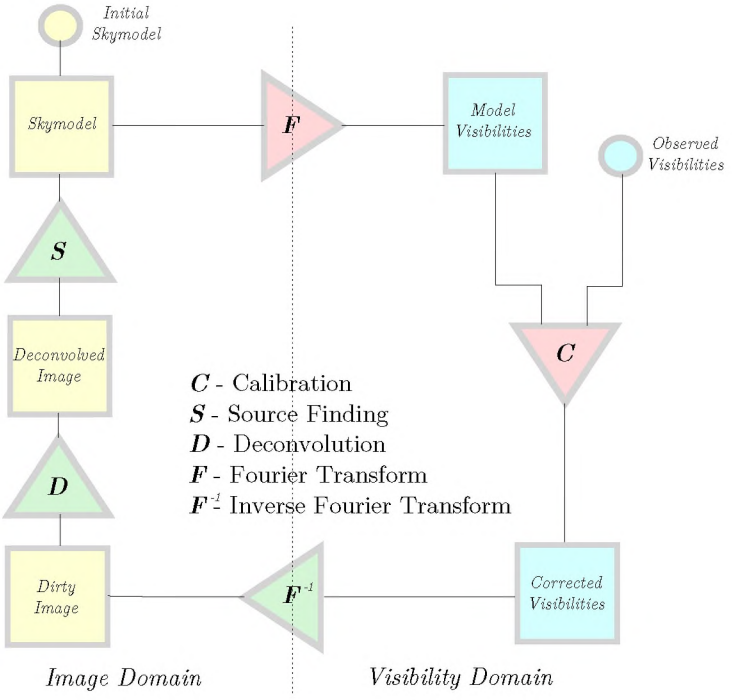

FIGURE 2.1: Selfcal flowchart

Selfcal can be performed using the following procedure:

1. Create an initial skymodel from the 1GC calibrated data.
2. Set your model to the initial skymodel and use it to calibrate the observed visibilities.
3. Image the corrected visibilities.
4. Run a source finder and make a new skymodel.
5. Return to Step 2 with your new skymodel or terminate if your are satisfied with your dynamic range.

Selfcal is generally used to compute direction independent complex antenna gains. Nowadays, this computation is mostly done using any of the optimization algorithms listed in Section 2.2. When self-calibration was first invented, it relied on closure relations (Smith, 1952; Jennison, 1958), instead of least squares and was called "hybrid-mapping". Readhead and Wilkinson (1978) were one of the first authors to coin the term "self-calibration". Ekers (1984) describes the different methods from adaptive optics through closure relations which led to the discovery of self-calibration. Self-calibration has proven to be very successful over the years and has made high dynamic range images possible.

2.3.3 Third Generation Calibration (3GC)

First and Second generation calibration discussed above focused mainly on solving DIEs thereby neglecting DDEs. With the wide field of views of current and future generation of radio telescopes such as the Low Frequency Array (LOFAR; Van Haarlem *et al.*, 2013), SKA and the Expanded Very Large Array (EVLA; Perley *et al.*, 2011), DDEs can no longer be ignored. This poses new challenges in calibration and calibration is currently moving into the 3GC era. 3GC techniques are calibration techniques used to solve for DDEs. 3GC techniques can be loosely classified into *Physics based* approaches and *Heuristic-only* approaches.

Physics based approaches are used when the underlying physical phenomenon causing the DDEs is known. The identified phenomenon is then modelled, parametrized and included in the RIME during calibration. Mitra *et al.* (2015) modelled the antenna primary beam and incorporated it in the calibration of the Jansky Very Large Array (JVLA) observations of the 3C417 field and obtained an unprecedented dynamic range of $5,000,000:1$ (the differential gain method was also applied in the data reduction). The image is shown in Figure 2.2. Other physics based approaches for direction dependent calibration include Pointing-Selfcal (Bhatnagar *et al.*, 2004), Kalman filters (Tasse, 2014) and AW projection (Bhatnagar *et al.*, 2008). The latter is actually an imaging based approach to correct for DDEs.

Heuristic based approaches are used when no phyiscal model exists for the specific DDE. Here the sources suffering the most from this DDE are identified and an extra Jones term is added to include the effects which are solved for during calibration. One such approach is *Peeling* proposed by Noordam (2004). Peeling solves for DDEs by correcting the effects towards each source separately in decreasing order of brightness. Each time the DDEs are solved towards a source, the source is subtracted and the process is repeated. The peeling algorithm is computationally expensive and the gain solutions are

sometimes contaminated (Smirnov, 2011). Smirnov (2011) proposed an approach called *differential gains* which prevents gain contamination by solving for the DIEs and DDEs simultaneously. For the differential gain method the RIME is rewritten explicitly as

$$\boldsymbol{V}_{pq} = \boldsymbol{G}_p \left(\sum_s \Delta \boldsymbol{E}_{sp} \mathcal{B}_{spq} \Delta \boldsymbol{E}_{sq}^H \right) \boldsymbol{G}_{\boldsymbol{q}}^{\boldsymbol{H}} \tag{2.40}$$

where $\Delta \boldsymbol{E}_{sp}$ and $\Delta \boldsymbol{E}_{sq}^H$ are the differential gains associated with source s and the antennas p and q respectively. Using differential gains Smirnov (2011) obtained a dynamic range record of about 1.6 million on the JVLA observations of the 3C147 field. Figure 2.2 shows the differences in a portion of an image before and after the use of differential gains.

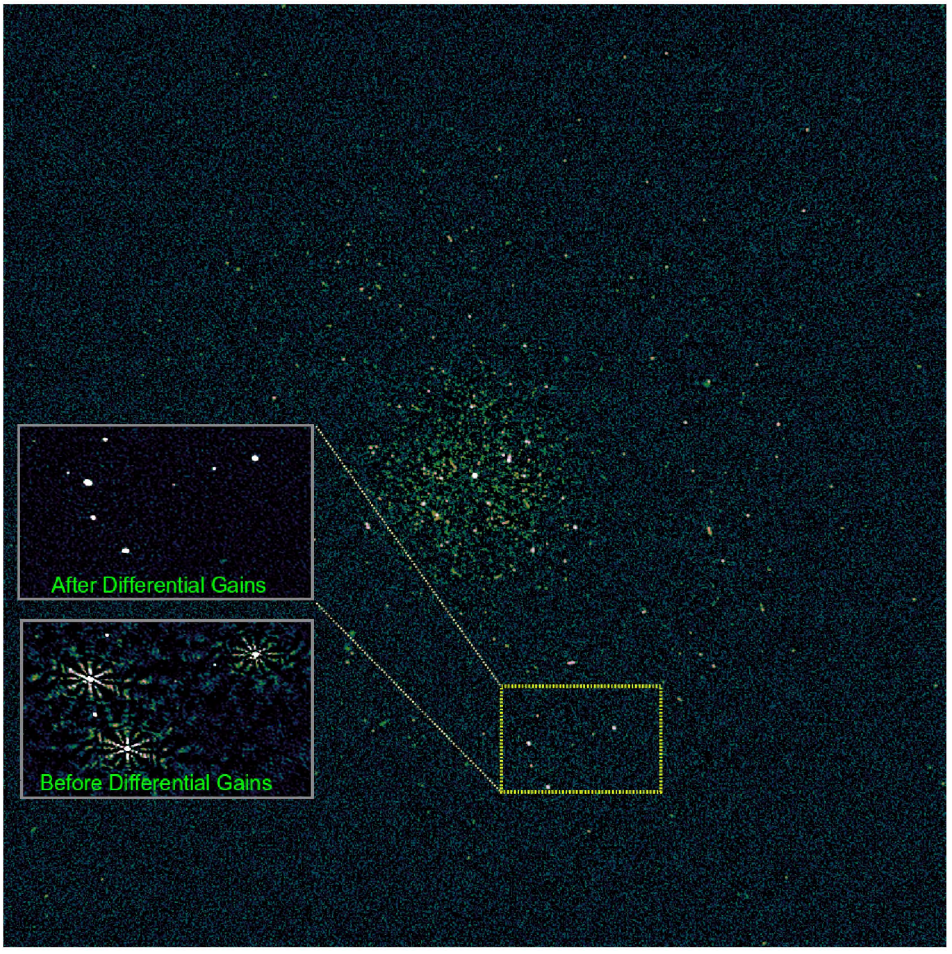

FIGURE 2.2: Differential gains and primary beam correction applied to the 3C147 field. (courtesy of O.M. Smirnov)

2.4 Calibration Artefacts

Calibration artefacts are systematics which result from "poor" calibration and cause imperfections in the final images. These include generation of spurious source components, deformations in the structures of extended sources, elimination and/or suppression of real source components (Linfield, 1986; Wilkinson *et al.*, 1988; Martí-Vidal and Marcaide, 2008). Calibration artefacts generally occur due to two factors:

- Incorrect modelling of the various propagation effects such as the modelling of the antenna primary beam or the modelling of ionospheric and tropospheric effects.
- Sky model errors i.e. missing or incorrect flux in our calibration sky model.

In the past few years Grobler *et al.* (2014); Wijnholds *et al.* (2016); Grobler *et al.* (2016); Patil *et al.* (2016) and Barry *et al.* (2016) have done extensive work on explaining the formation of a particular class of artefacts called *ghost sources* which result from sky model errors. Grobler *et al.* (2014) developed a theoretical framework to predict the ghost pattern for a simple two sources scenario (a field with a 1 Jy source at the phase center, a 0.2 Jy source at an offset position and only the 1 Jy source was included in the calibration sky model) using the Westerbork Synthesis Radio Telescope (WSRT) configuration. The theoretical framework was developed using the Alternating Least Square (ALS) algorithm (Boonstra and Van Der Veen, 2001) and simulations were performed using both the ALS algorithm and a Least Squares (LS) optimization algorithm (to be precise the LM algorithm) and the results were compared. Below are a few results from Grobler *et al.* (2014) which will be useful for the rest of this thesis:

- For both the ALS and the LS cases the bright ghost sources appeared at the same positions. This result was in agreement with their theoretical prediction.
- The ghost pattern from the ALS and the LS were qualitatively similar, but showed different amplitudes. This was suspected to be due to the slight differences in the optimization problems solved by both algorithms.
- For both cases most of the ghost sources had negative fluxes, very few had positive fluxes and their fluxes were very weak. This explains the fact that calibration artefacts are generally very faint and buried in the residual noise.
- The 0.2 Jy source which was not included in the calibration sky model experienced a flux suppression of $\approx 13\%$. This value is consistent with the expected rates from WSRT when calibrated with an LS algorithm. Further investigations by Nunhokee (2015) showed that the suppression rate for direction dependent calibration could sufficiently be reduced by using longer solution intervals.

Grobler *et al.* (2014) mainly used WSRT which is a very redundant array. The array geometry was judged to play an important part in the generated ghost pattern. Wijnholds *et al.* (2016) extended this work to more general array layouts. Grobler *et al.* (2014) postulated that the flux of the ghost sources were independent from the flux of the modelled source and were linearly related to that of the unmodelled source but was unable to get an expression for the flux of the ghost sources. Wijnholds *et al.* (2016) used KAT-7's configuration for their theoretical predictions and derived closed form expressions for the fluxes and positions of the brightest ghosts.

Patil *et al.* (2016), Barry *et al.* (2016) and Ewall-Wice *et al.* (2016) used a different approach from Grobler *et al.* (2014); Wijnholds *et al.* (2016) and Grobler *et al.* (2016) and studied the effects of unmodelled sources on power spectrum measurement and the effects on foreground subtractions for Epoch of Reionization (EoR) purposes. Patil *et al.* (2016) performed simulations with the Low Frequency Array (LOFAR) where they did not model extended emission and obtained an increase in noise due to the unmodelled extended emission. Patil *et al.* (2016) also showed that short baselines were the most affected and that the effects could considerably be reduced by only keeping long baselines. Barry *et al.* (2016) performed simulations with unmodelled point sources and presented the minimum requirements for sky model completeness for EoR detections. Ewall-Wice *et al.* (2016) studied the effects of sky model errors on the 21 cm power spectrum measurements and proposed a method to reduce these effects.

2.5 Summary

In this chapter we described calibration, which is the process of solving for all the propagation factors that corrupt measured visibilities. We showed that calibration is an optimization problem and discussed the RIME which is a mathematical formalism used to model propagation effects during calibration. We followed up by describing two calibration algorithms, namely, the LM and the StEFCal algorithms, which illustrate two different approaches which can be used during radio interferometric calibration. Furthermore we discussed some developments in calibration strategies which we described in three calibration generations. Lastly we introduced calibration artefacts which are systematics produced during calibration. In the next chapter we study the effects of ignoring long-term variable sources during calibration.

Chapter 3

Calibration Artefacts from long-term Variable Sources

Despite the evidence of existing variable sources (Heeschen *et al.*, 1987; Ulrich *et al.*, 1997; Kadota *et al.*, 2012), apart from variability search surveys such as Stewart *et al.* (2016) and Rowlinson *et al.* (2016), current calibration approaches do not yet routinely incorporate source variability. Calibration using static source models for variable sources will introduce systematic errors in visibility data resulting in calibration artefacts in the images. This chapter, which is the core of this thesis, investigates how long-term variable sources affect calibration results by studying the rms or noise of residual visibilities.

long-term variable sources here are defined to be sources which vary over long time scales such as days and weeks. Here, we do not use any advanced calibration technique such as self calibration. The goal of this chapter is to show that future reduction pipelines can not rely on static source models unless the target field contains no variable source, but instead would require some sort of automatic self calibration. Self calibration would be required to reduce the amount of artefacts in images resulting from sky models errors, such as missing sources and errors in the fluxes of variable sources. We extend the framework proposed in Grobler *et al.* (2014) and Wijnholds *et al.* (2016). An important aspect we consider is what happens when we model sources with higher flux densities than their true flux densities. We obtain a similar but symmetrically opposite scenario to when the flux is underestimated during calibration. Furthermore we investigate how the generated artefacts combine together when various such residuals are stacked together. We performed the following two sets of experiments.

- Normal simulations: In this section we perform simulations of a field containing a single variable source whose light curve (i.e. its flux density variation over time) is

either normally distributed or skew distributed. We study how the skewness of the light curve affects the rms images particularly those of stacked images.

- Realistic simulations: Here we extended the simulations above to real life scenarios where the variable source has a realistic light curve and the calibration model for the variable source were progressively updated during each simulation. This was also extended to fields containing multiple variable sources. Note that we used light curves generated from optical astronomy observations here and this should not affect our results as we expect light curves from radio astronomy observations to have similar statistical properties.

We begin this chapter by describing the various parts of the pipeline we used to perform the experiments in section 3.1. In Section 3.2 we present the normal simulations and its results. We follow up with the realistic simulations and its analysis. Finally we discuss the conclusions from both experiments in Section 3.4 and provide the overall summary of the chapter in Section 3.5.

3.1 Simulation Pipeline

For both sets of experiments we used a python-based pipeline and its main functionalities are demonstrated in Figure 3.1. The pipeline takes two inputs namely; an observation sky model corresponding to the true sky model of the field being observed and a calibration sky model corresponding to the sky model used during calibration.

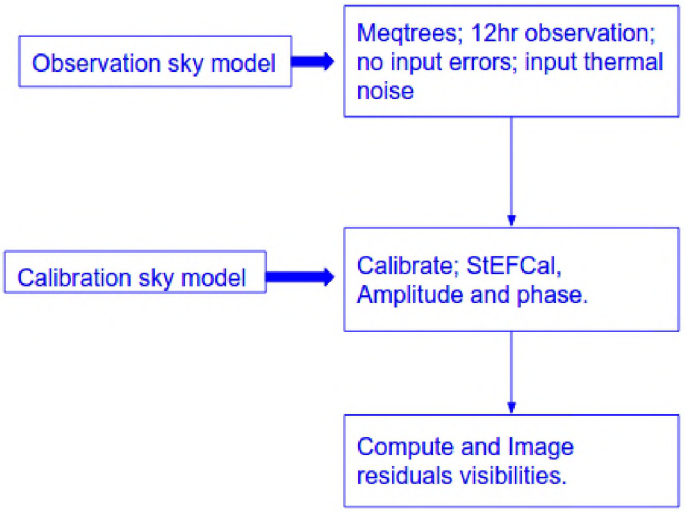

FIGURE 3.1: Flowchart depicting the main functionalities of the simulation pipeline.

3.1.1 Visibility Simulations

For each simulation, we simulate visibilities of a 12 hour observation of the input sky model using MeqTrees (Noordam and Smirnov, 2010). We used KAT-7 antenna configuration for these simulations. The input noise was computed from the system equivalent flux density ($SEFD$) of KAT-7 via the following equations,

$$SEFD = \frac{2k_B T_{sys}}{\eta A} \tag{3.1}$$

$$\sigma_{rms} = \frac{SEFD}{\sqrt{2N(N-1)\Delta v \Delta t}} \tag{3.2}$$

where k_B is the Boltzmann's constant, 1.38×10^{-32} m^2 kg s^{-2} K^{-1}, T_{sys} is the system temperature of a KAT-7 antenna $\approx$ 35K, $\eta = 0.66$ is the efficiency of KAT-7 antenna, $A = 113.10$ m^2 is the area of a KAT-7 antenna, $N = 7$ is the number of KAT-7 antennas, $\Delta v = 237$ MHz is the bandwidth we used for the simulations and $\Delta t = 60$ s is the integration time we used for the simulations. These computations gave us an input noise with mean 0 Jy and standard deviation, $\sigma_{rms} \approx 0.00845$ Jy.

Since we were only interested in studying the effect of the "poorly" modelled variable source, we didn't include any other form of error such as antenna gains or primary beam errors in the simulated visibilities.

3.1.2 Calibration and Residuals

Each of the simulated observations are calibrated with its corresponding calibration sky model as explained in Chapter 2. Because the simulated observations are error free we only solve for the direction independent antenna gains, $\boldsymbol{G}$ as follows

$$\underset{\boldsymbol{G}}{\operatorname{argmin}} \|\boldsymbol{R} - \boldsymbol{G}\boldsymbol{M}\boldsymbol{G}^H\|^2 \tag{3.3}$$

where $\boldsymbol{R}$ represents the observed visibilities, $\boldsymbol{M}$ represents the modelled visibilities, the superscript $(\cdot)^H$ denotes the Hermitian or conjugate transpose and $\|\cdot\|$ denotes the Frobenius norm.
The StEFCal algorithm (Salvini and Wijnholds, 2014) which was discussed in Section 2.2.2 was used to compute the antenna gains.
To study the noise in the final images, we compute three residual visibilities, the *corrected residuals*, the *distilled residuals* and the *ghost-subtracted residuals*.

- *Corrected residuals*: These provide a measure of how well the calibration was performed. They are computed by taking the difference between the corrected

visibilities and the model visibilities.

$$\boldsymbol{V}_{res}^{corr} = \boldsymbol{G}^{-1}\boldsymbol{R}\boldsymbol{G}^{-H} - \boldsymbol{M} \tag{3.4}$$

where $\boldsymbol{V}_{res}^{corr}$ represents the corrected residuals.

- *Distilled residuals*: These are not computed during calibration, but are evaluated when attempting to isolate calibration artefacts. Grobler *et al.* (2014); Wijnholds *et al.* (2016); Grobler *et al.* (2016) have used these residuals to study and predict the fluxes of the different ghost sources resulting from calibration with incomplete sky models. They are computed as follows

$$\boldsymbol{V}_{res}^{dist} = \boldsymbol{G}^{-1}\boldsymbol{R}\boldsymbol{G}^{-H} - \boldsymbol{R}_{\text{free}} \tag{3.5}$$

where $\boldsymbol{V}_{res}^{dist}$ represents the distilled residuals and $\boldsymbol{R}_{\text{free}}$ are the noise free observed visibilities, i.e. during each observation simulation, we perform a parallel simulation in which no noise is included.

- *Ghost-subtracted residuals*: They are computed as follows

$$\boldsymbol{V}_{res}^{ghost} = \boldsymbol{G}^{-1}\boldsymbol{R}\boldsymbol{G}^{-H} - \boldsymbol{R}_{\text{free}} - \boldsymbol{V}_{\text{ghost}} \tag{3.6}$$

where $\boldsymbol{V}_{res}^{ghost}$ represents the ghost-subtracted residuals and $\boldsymbol{V}_{\text{ghost}}$ are the approximated visibilities of the *secondary suppressor*. The secondary suppressor (Wijnholds *et al.*, 2016) is the ghost source which forms at the position of an unmodelled source and causes a reduction in the flux of the latter. The secondary suppressor is the brightest ghost and contributes most of the power from the artefacts. Subtracting this enables us to have a measure of the amount of power from all the other fainter artefacts. From Wijnholds *et al.* (2016) the flux of the secondary suppressor is defined as

$$f_{\text{sup}} = f_{\text{unm}}\left(\frac{2}{N} - \frac{1}{N^2}\right) \tag{3.7}$$

where f_{sup} is the flux of the secondary suppressor, f_{unm} is the flux of the unmodelled source and N is the number of antennas in the array. Here we assumed the flux of the secondary suppressor to be the peak flux at the position of the unmodelled source in the distilled residuals. We computed $\boldsymbol{V}_{\text{ghost}}$ by simulating the visibilities of a sky model containing only the secondary suppressor using MeqTrees.

3.1.3 Sky Models

The goal of these experiments was to simulate multiple observations of fields containing variable sources and to study the effects of the variable sources when they were modelled as non-variable sources. Thus for these experiments we needed sky models containing variable sources. Our approach was to first generate an initial sky model, from this model we selected 10 sources as variable and generated light curves for these variable sources. The light curves for the variable sources were generated depending on the specific experiment we were performing. In each case the initial sky model was generated as follows. A random sky distribution of 30 sources covering a 1° field of view was chosen. The sources' positions were uniformly distributed across the field and the flux values followed the same translated pareto distribution in Nunhokee (2015) defined as

$$A_p(x) = \frac{a}{(x+1)^{a+1}}, \tag{3.8}$$

where $A_p(x)$ is the probability density function of the pareto distribution, x is the random variable representing the flux of the variable source, a is the shape parameter.

3.2 Normal and Skew Simulations

In this experiment the flux of the variable source was either normally or skew distributed relative to the model flux value. All variable sources had a variability index of 30% defined as follows

$$VI = \frac{\sigma}{\mu} \times 100 \tag{3.9}$$

$$\sigma = \frac{VI}{100} \times \mu \tag{3.10}$$

where σ is the standard deviation of the light curve, μ is the mean and VI is the variability index. Starting with the initial sky model generated as described in Section 3.1.3, we generated the various true sky models containing the variable source and their corresponding calibration sky models as follows. The true sky models here correspond to the exact sky model from which the observed visibilities are simulated. Given that we were studying long-term variable sources, the fluxes of the variable sources were held constant in each sky model but allowed to vary across the sky models.

1. The mean flux density of the variable source was chosen to be its flux density in the initial sky model. Its standard deviation was computed from its mean flux density via Equation 3.10.

2. We generate 100 random numbers following a normal distribution having the mean and standard deviation computed in Step 1.

3. We generate 100 sky models from the initial sky model in which the flux density of the variable source is changed in each case to correspond to each of the values of the random sequences from Step 2.

4. We compute a histogram of the random sequences using 20 bins and generate 20 calibration sky models from the initial sky model in which the flux density of the variable source is changed to correspond to each of the 20 bin centers.

The plot in Figure 3.2 shows the probability density function (pdf) of the variable source light curve and the different model flux values (the flux of the variable source in the calibration sky model).

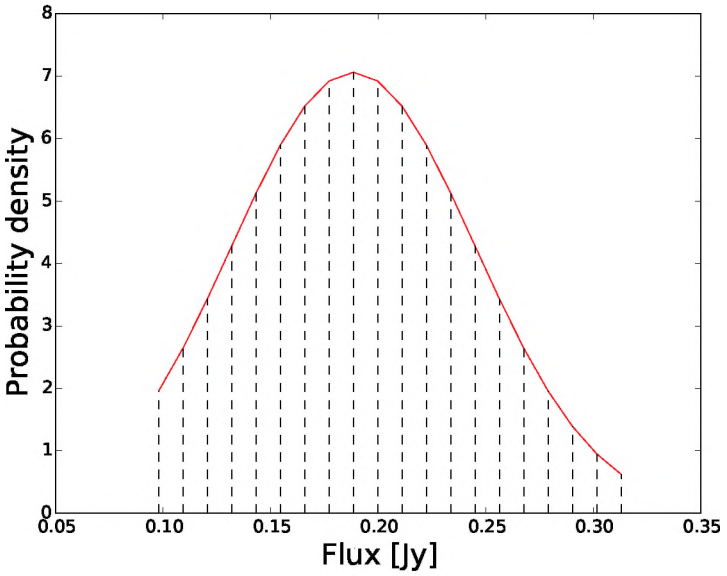

FIGURE 3.2: Probability density function of the variable source light curve. The red dotted line is the probability density function of the variable source light curve and the black dotted lines are the different flux values used to model it in the different calibrations.

Using the pipeline described in Section 3.1 the following experiment was performed:

- Simulate observations of the observation sky models as described in Section 3.1 (i.e. 100 observations for our 100 observation sky models).

- Calibrate all of the simulated observations using each of the 20 calibration sky models. We used the StEFCal algorithm for the calibration.

- Compute and image the corrected, distilled and ghost-subtracted residuals for all the simulations.

3.2.1 Ghost Sources and Suppression Analysis

As briefly introduced in Section 2.4, Grobler *et al.* (2014) and Wijnholds *et al.* (2016) have performed extensive studies on ghost sources which result from calibration with incomplete sky models. One of the main results from Grobler *et al.* (2014) was that the brightest ghost source in the distilled residuals always forms at the same position (i.e. the position of the unmodelled source). This ghost is the secondary suppressor, which defines the amount of flux lost by the unmodelled source. Nunhokee (2015) showed that the flux of this brightest ghost source was related and approximately equal to the amount of flux suppressed from the unmodelled flux. Nunhokee (2015) further demonstrated that the suppression rate is ≈ 0.14 for Westerbork Synthesis Radio Telescope (WSRT) configuration. Wijnholds *et al.* (2016) derived it to be $\approx \frac{2}{N}$ (for any array layout) where N is the number of antennas.

Our first investigation was to check if the suppression result held for our variable source scenario. In this case the calibration sky model is incomplete due to the variable source which is not properly modelled. The variable source can be viewed as two sources at the same position with one modelled and the other unmodelled. We essentially checked if the secondary suppressor from the amount of unmodelled flux of the variable source agrees with Wijnholds *et al.* (2016).

The plots in Figure 3.3 are images of the corrected and distilled residuals obtained from the experiment which confirms that the brightest ghost source always forms at the same position. From these plots we can see the distinct ghost close to the center of all the images. in images 3.3a and 3.3b where the flux of the variable source is underestimated, the distilled image 3.3a has a bright negative ghost at its center. This is the suppression ghost and the magnitude of its flux corresponds to the amount of flux suppressed from the variable source. The corrected residuals (3.3b) are dominated by positive pixels. This indicates some flux was not accounted for in the calibration. The magnitude of the bright spot at the center corresponds to the amount of unmodelled flux which may be recovered if further calibration such as self calibration is performed (of course baring the amount of flux which was suppressed).

On the other hand the images 3.3c and 3.3d correspond to a simulation where the flux of the variable source is overestimated. This is rarely studied and is one of the novel contributions of this thesis, as most often research is focused on studying the effects of missing flux rather than the case of having more flux in the calibration sky model than

in the actual sky. The distilled image 3.3c has a bright positive ghost at the position of the unmodelled source. This is analogue to the secondary suppressor and we call it the *secondary amplification ghost*. It corresponds to the amount by which the flux of the variable source will be increased. The corrected residuals in this case are dominated by negative pixels. This indicates more flux is being considered in the calibration model than the data actually contains.

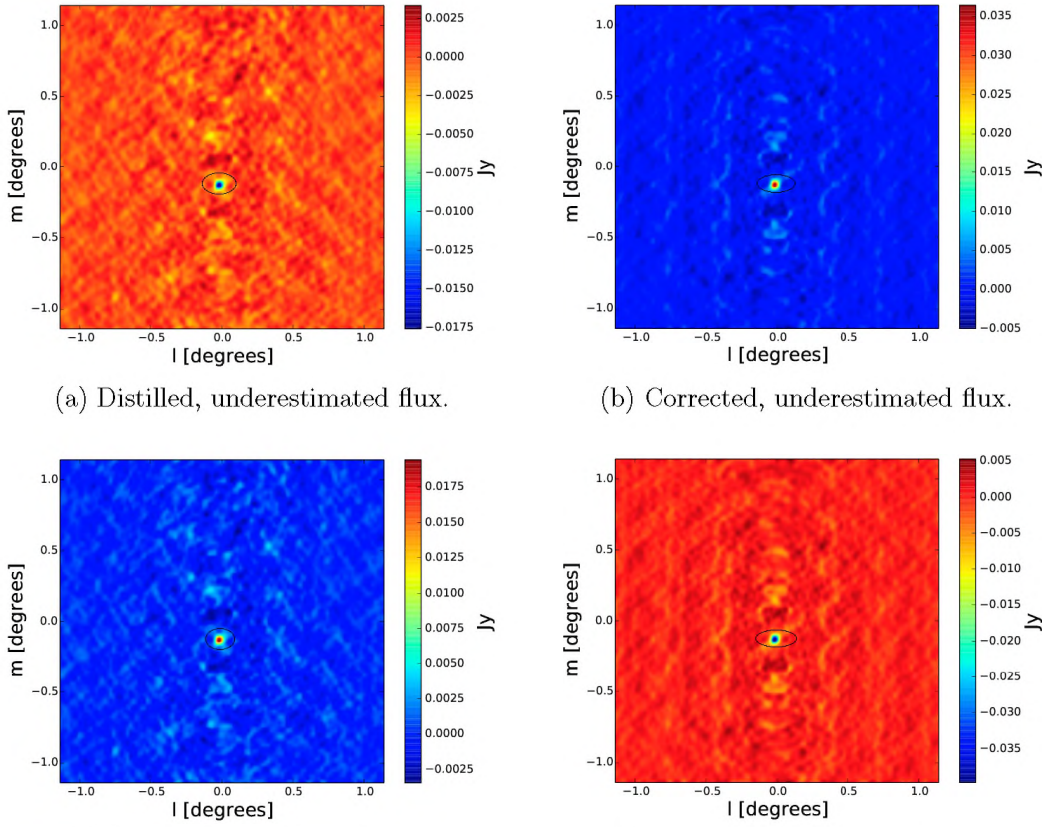

(a) Distilled, underestimated flux.

(b) Corrected, underestimated flux.

(c) Distilled, overestimated flux.

(d) Corrected, overestimated flux.

FIGURE 3.3: Distilled and corrected residual images for two simulations. The top plots corresponds to a case where the flux of the variable source is underestimated. The bottom plots correspond to a case where the flux of the variable source is overestimated. The amplification and suppression ghosts are shown in the black ellipses.

The next step was to investigate if the suppression rates were constant and consistent with Wijnholds *et al.* (2016) theoretical rate. Figure 3.4 is a plot of the measured suppression rates and the theoretical or expected suppression rate. For KAT-7, the suppression rate is expected to be $\frac{2}{7} \approx 0.285$. Figure 3.4 shows the suppression rate is approximately constant as we expected. We measured suppression rates slightly above the expected rate 0.285. This result agrees with Wijnholds *et al.* (2016) predictions, even for partially modelled sources, as is the case of variable sources. The slight differences in suppression rates probably result from the uncertainties in measuring the fluxes of the

suppression ghosts. Moreover the ghost flux for simplicity was assumed to be the peak flux at its position, not the integrated which should be slightly higher, thus reducing the slightly higher measured suppression rates.

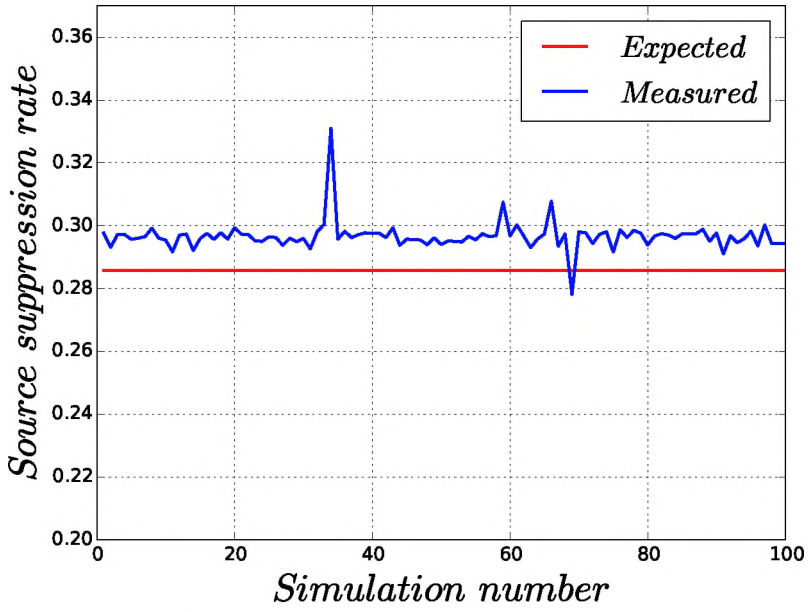

FIGURE 3.4: Measured suppression rate in blue and expected suppression rate in red showing almost constant suppression rates. We can see that the measured suppression rate here agrees with Wijnholds *et al.* (2016) predicted rate.

Thus we can draw the following two conclusions from the ghost sources analysis:

- As pointed out previously by Grobler *et al.* (2014) and Wijnholds *et al.* (2016) when a source is underestimated (i.e. it is modelled with a flux density lower than its actual flux density), calibration attempts to recover the unmodelled flux but can only recover a certain percentage. The unrecovered flux forms a ghost source whose flux is proportional to the amount of unrecovered flux at the position of the source.

- When a source is overestimated (i.e. it is modelled with a flux density higher than its actual flux), calibration attempts to compensate for the extra flux. This leads to the generation of an amplification ghost whose flux is proportional to the amount of extra flux included in the calibration model at the position of the source. This study shows that this is a similar but symmetrically opposite scenario to the underestimated flux scenario. Thus analogously to a source whose flux is underestimated, a source whose flux is overestimated will have its flux increased by $\approx \frac{2}{N}\%$ of the overestimated flux.

3.2.2 Stacking and Noise Analysis.

Stacking is a technique used in radio surveys to reduce the rms of images and produce high dynamic range images (Lindroos *et al.*, 2015). This technique works under the assumption that the noise follows a normal distribution. The rms of normally distributed noise averages as $\sigma \propto \frac{1}{\sqrt{M}}$ where σ is the rms and M is the number of images stacked together when several normally distributed images are stacked together. We stacked (averaged) residual images from the same set of simulations. Before studying the noise we first examine the final stacked images visually. Given that we are only interested in the noise, we focus on the corrected and ghost-subtracted residuals. Since the secondary suppressor and amplification ghost always forms at the position of the unmodelled source, the stacked image also contains a bright ghost at the position of the unmodelled source. The flux of this ghost source is equal to the average flux of all the secondary and amplification ghosts from the different images stacked together. Figure 3.5 shows the stacked corrected residuals for two different scenarios and the probability density function of the variable source light curve with the amount of flux used to model it during calibration. Figure 3.5a is the stacked corrected residuals image. The black dotted line in Figure 3.5b marks the flux used to model the variable source in this experiment and the red curve is the probability density function of the light curve. Here we can say that the variable source light curve is right skew distributed with respect to this calibration model flux value. Thus overall the final stacked image is similar to that of a single simulation in which the flux of the variable source is underestimated. Figure 3.5c is a final stacked corrected residuals for an experiment in which the variable source light curve is left skew distributed with respect to the calibration flux density value as shown in Figure 3.5d. Thus overall the final stacked image is similar to that of a single simulation in which the flux of the variable source is overestimated.

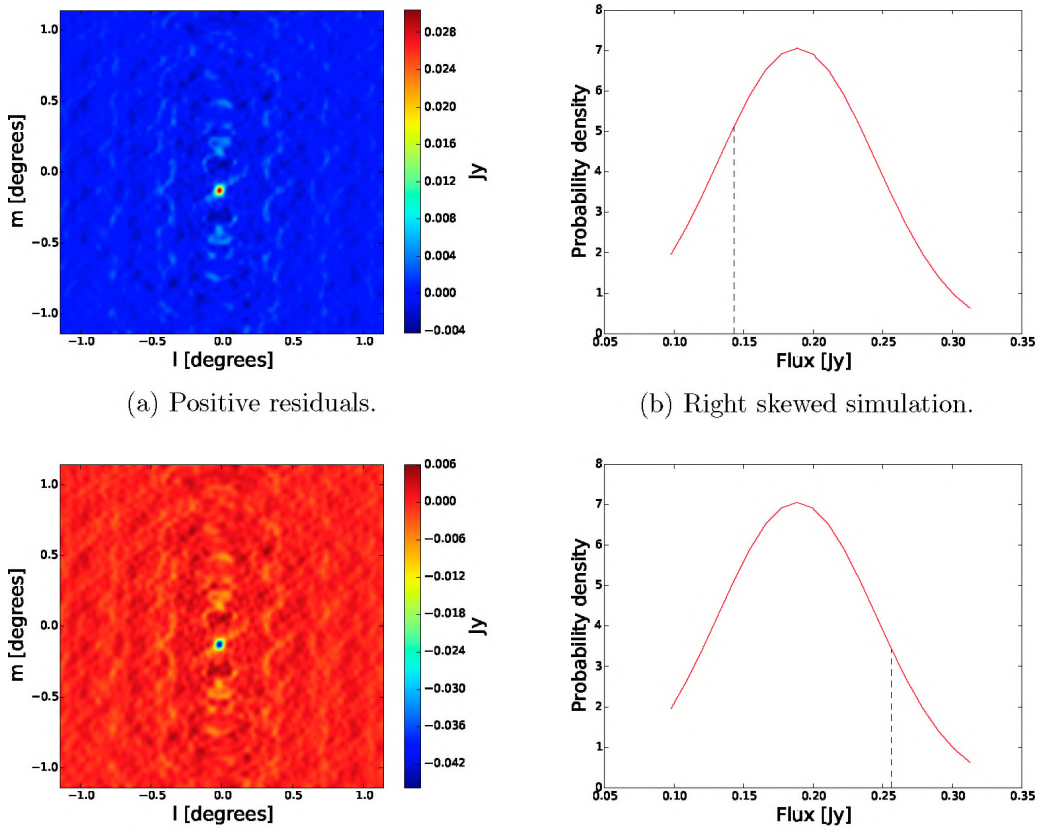

(a) Positive residuals.

(b) Right skewed simulation.

(c) Negative residuals.

(d) Left skewed simulation

FIGURE 3.5: Plots of final stacked residual images on the left and the probability density function with the corresponding flux density value used to model the variable source in the experiment on the right.

This result is further illustrated with the plot in Figure 3.6. This is a plot of the absolute average flux of the bright ghost (secondary suppressor or secondary amplification) against the skewness of the variable source light curve with respect to the calibration flux value. Here the skewness is computed as follows:
For a sequence, S_i, its skewness, γ with respect to a value, t is defined as

$$\gamma = \frac{\frac{1}{n}\sum_i^n (S_i - t)^3}{\left[\frac{1}{n-1}\sum_i^n (S_i - t)^2\right]^{\frac{3}{2}}} \tag{3.11}$$

where n is the length of the sequence, S_i.

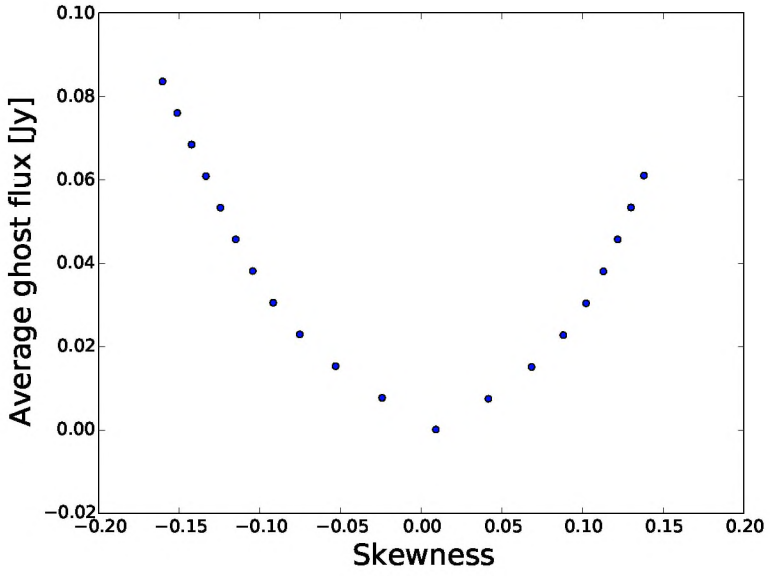

FIGURE 3.6: The absolute average flux of the bright ghost against the skewness of the variable light with respect to the calibration flux density value.

From Figure 3.6 we observe that if the skewness is close to zero, i.e if the light curve has a normal distribution with respect to the calibration flux value the brightest ghost sources from the various images will completely cancel out. This is because the summed flux of the brightest positive ghost sources will be approximately equal to that of the brightest negative ghost sources. On the other hand if the light curve has a skew distribution both left or right the average flux of the brightest ghost source will be much greater than zero.

Noise in images is defined as the random variation in the brightness information of objects. In radio astronomy this is the variation from all non radio sources of emissions present in the image. Thus in computing the corrected residuals we subtracted all radio emission from the image. However, since the variable source was not correctly modelled, this led to the formation of a bright ghost source in the residual image; in order to get a better noise estimate, we have to look at the ghost-subtracted residuals.

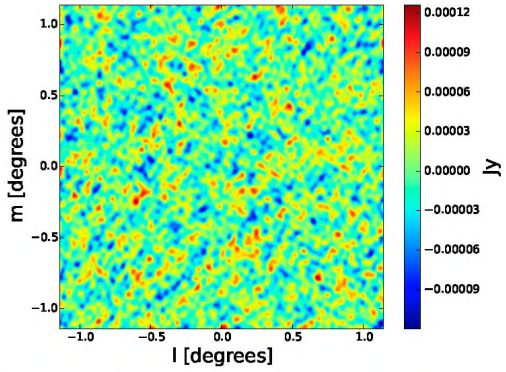

(a) Pure noise obtained from calibration with complete sky model.

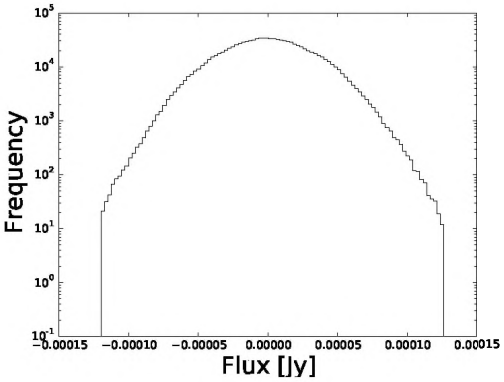

(b) Histogram plot.

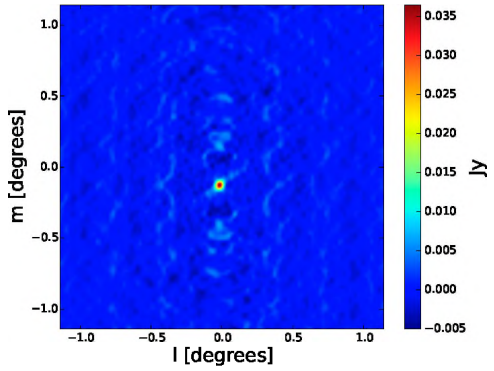

(c) Noise when the variable source is underestimated.

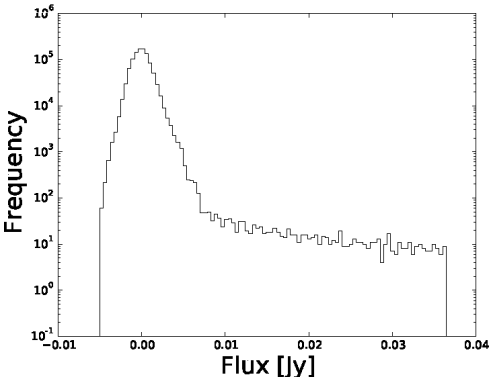

(d) Histogram plot.

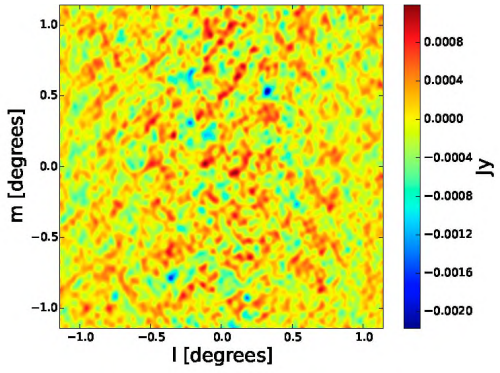

(e) Noise after subtraction of ghost source for underestimated flux.

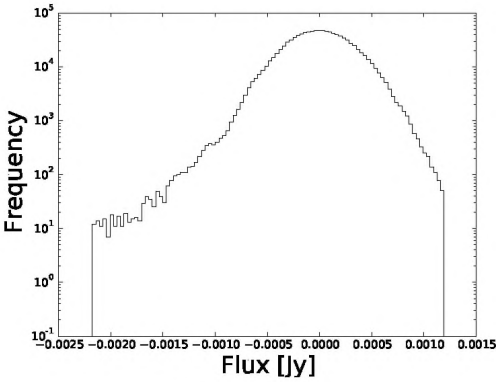

(f) Histogram plot.

FIGURE 3.7: Noise images on the left and histogram plots on the right showing the effects on the residuals distribution when the variable source is underestimated.

Noise in radio images is generally quantified using the root mean square (rms) defined as,

$$\sigma = \sqrt{\frac{1}{N}\sum_{i=1}^{N}(x_i - \mu)^2}, \tag{3.12}$$

where σ is the rms, x is the flux density of each pixel in the image, N is the number of pixels and μ the mean of x.

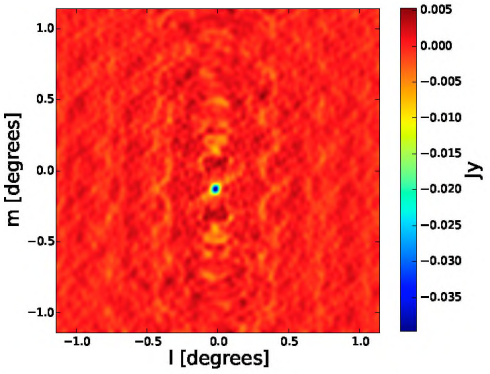

(a) Noise when the variable source is overestimated.

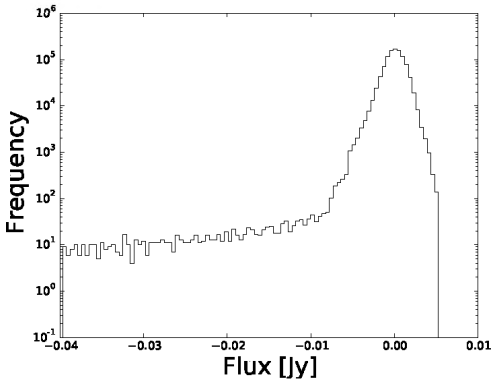

(b) Histogram plot.

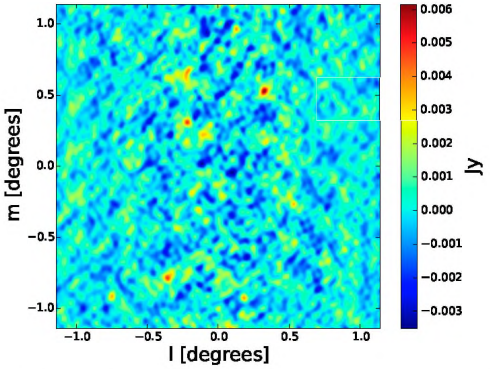

(c) Noise after subtraction of ghost source for overestimated flux.

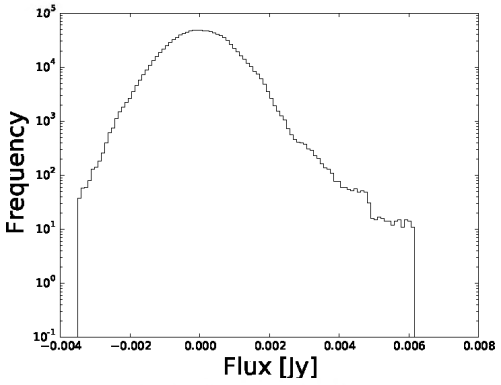

(d) Histogram plot.

FIGURE 3.8: Noise images on the left and histogram plots on the right showing the effects on the residuals distribution when the variable source is overestimated.

Ideally we want the noise to be normally distributed, but when calibration is done with incomplete sky models, calibration artefacts are introduced in the form of ghost sources in the noise. These artefacts cause the noise not to be normally distributed. The histogram plots of corrected residual images in Figure 3.7 illustrate this. When calibration is done with a complete sky model the noise is almost normally distributed as shown in Figures 3.7a and 3.7b. When the sky model is incomplete as in our experiment with the variable source flux either being underestimated or overestimated, the residuals are skew distributed. When the variable source is underestimated during calibration, the tail of the skew residuals is to the right as shown with Figures 3.7c and 3.7d. Analogously when the variable source is overestimated during calibration, the tail of the skew residuals is to the left as shown with Figures 3.8a and 3.8b. Even the subtraction of the brightest

ghost sources from the residuals as illustrated in Figures 3.7e, 3.7f, 3.8c and 3.8d does not render the residuals completely normally distributed. This is because of the secondary artefacts which have not been removed. The tails in Figures 3.7f and 3.8d may also result from the imperfect subtraction due to the slight inaccuracies of the theoretical estimate.

Furthermore stacking the images does not significantly reduce the rms. As discussed earlier stacking the images does not necessarily imply the ghost sources introduced by the artefacts will cancel out. They only cancel out if the skewness of the variable source light curve relative to the calibration flux density value is close to zero. Figure 3.9 are plots of the rms against the number of images stacked together in logarithmic scales illustrating this point.

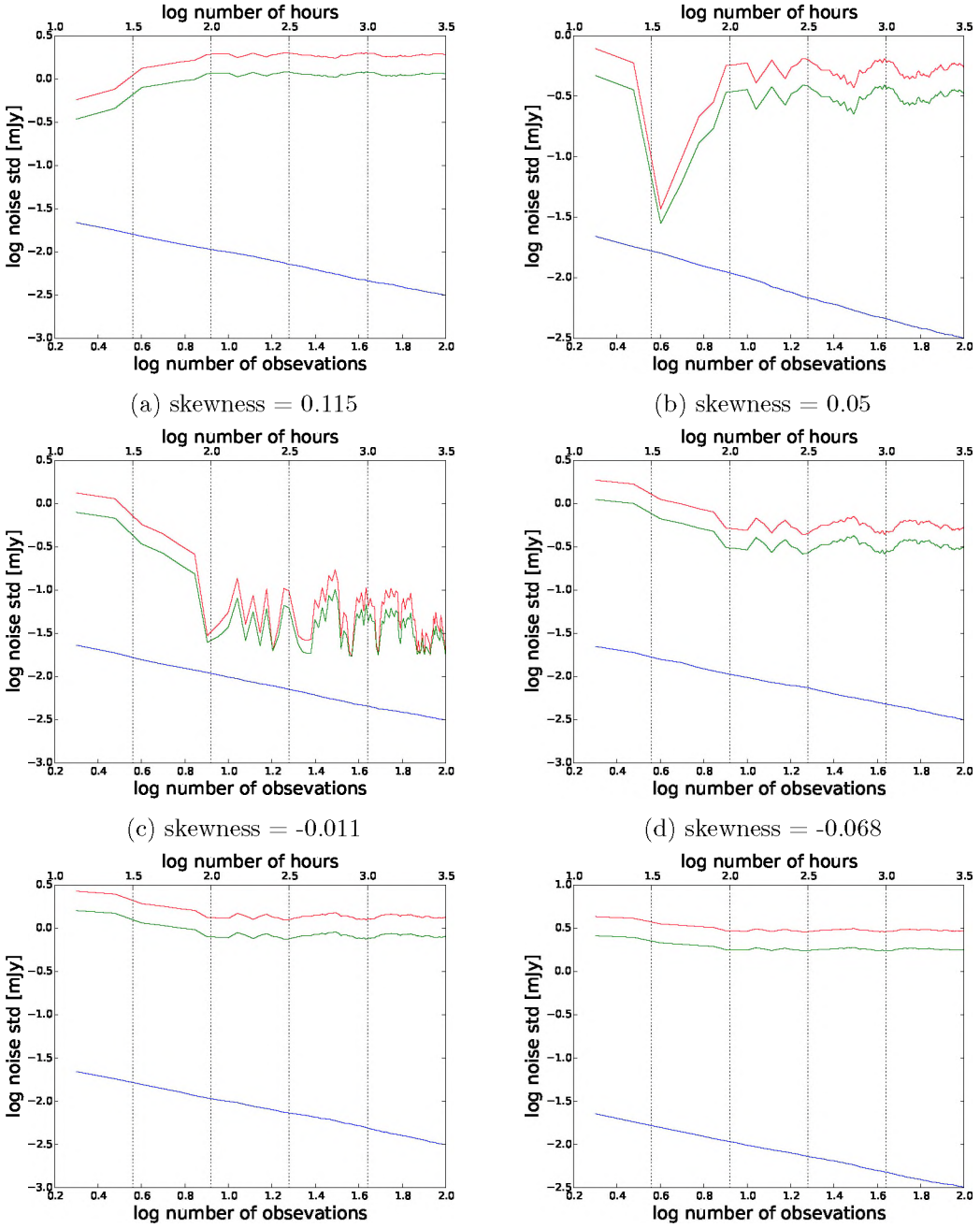

(a) skewness = 0.115

(b) skewness = 0.05

(c) skewness = -0.011

(d) skewness = -0.068

(e) skewness = -0.150

(f) skewness = 0.153

FIGURE 3.9: Plots of log rms of the stacked images against the log of number images stacked together for eight experiments. The blue curve corresponds to the noise from simulations in which the correct sky model is used for calibration. The red curve corresponds to the noise from the corrected residuals when an incomplete sky model is used during calibration. The green curve corresponds to the noise from the ghost-subtracted residuals when the incomplete sky model is used during calibration.

3.3 Realistic Experiment

In the previous experiment, the light curves of the variable sources followed a normal distribution. In this section we simulate more realistic light curves. In contrast to the previous simulations the same calibration model is not used across all the observations. In real life, calibration of a variable source will be done using our existing knowledge of the source. As in the previous experiment we start by generating the initial sky model as described in Section 3.1.3.

3.3.1 Generating Realistic Light Curves

For each variable source we generate its corresponding light curve using Connolly's python light curve generation package (Connolly, 2016). This tool allows the simulation of light curves with known statistical properties i.e. the power spectral density (PSD), probability density function (PDF), mean and standard deviation. It uses the algorithm described by Emmanoulopoulos *et al.* (2013). Throughout this experiment all variable source light curve PSD and PDF follow a Bending power law and a Gamma distribution with identical parameters respectively. These two functions are defined in Appendix A.

The initial flux densities of the variable sources were used as their mean values and their standard deviations were computed using Equation 3.10. The plots in Figure 3.10 show two such generated light curves.

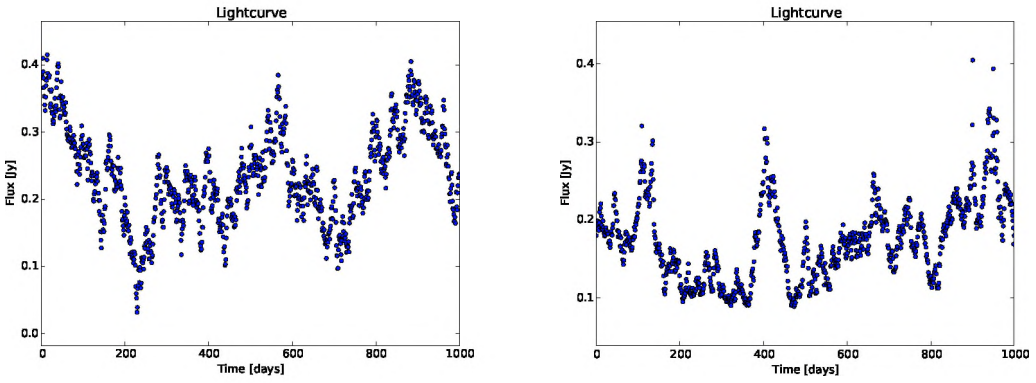

(a) (b)

FIGURE 3.10: Generated light curves for two variable source. Left the source has a mean of 0.3 Jy and a standard deviation of 0.09. Right the source has a mean of 0.2 Jy and a standard deviation of 0.06

3.3.2 Random Sampling

The light curves shown in Figure 3.10a and 3.10b were generated for a period of 1000 days. For this experiment we selected 80 random days and performed simulations corresponding to these days by forming the observation and calibration sky models as follows;

- For each observation day the true flux of the variable source was obtained from its light curve.
- For the first observation the flux of the variable source was modelled with the first flux value of its light curve.
- For the subsequent observations, the flux of the variable source was modelled with the mean of all the previous observed flux values including the one used for the first calibration.

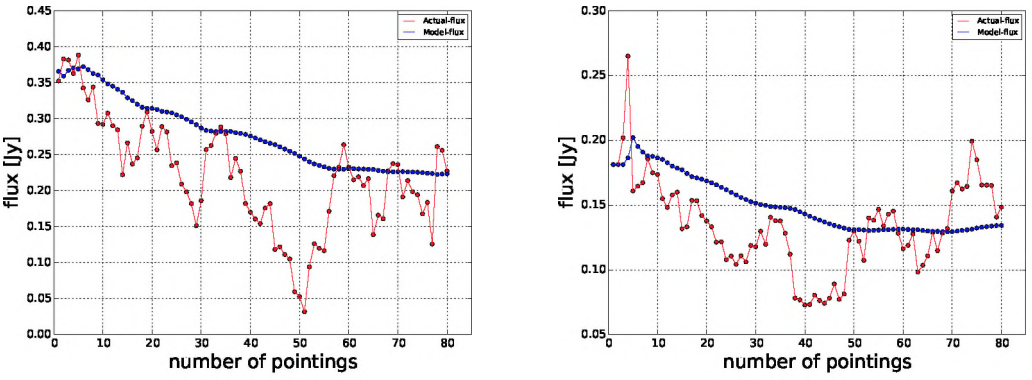

(a) (b)

FIGURE 3.11: Plots of the actual flux density, red and the model flux density, blue for two sources.

With this approach we use our previous knowledge of the variable source to model it in its subsequent observations by taking the average of the previous measured flux values for this source. Figure 3.11 are plots of the true flux densities and model flux densities for two sources used in the experiment.

3.3.3 Simulations

The simulations were done similarly as in Section 3.2 with the following few exceptions

- Each simulated observation was calibrated with a different calibration sky model.

- Here we only focus on the noise, therefore only the corrected and ghost-subtracted residuals were computed and used for further analysis.

3.3.4 Results

3.3.4.1 Fields with a Single Variable Source

The corrected residuals are similar to those in the previous sections. They are skew distributed depending on the difference between the true flux density value of the source and the calibration flux density value. This is illustrated with the plots in the Figure 3.12.

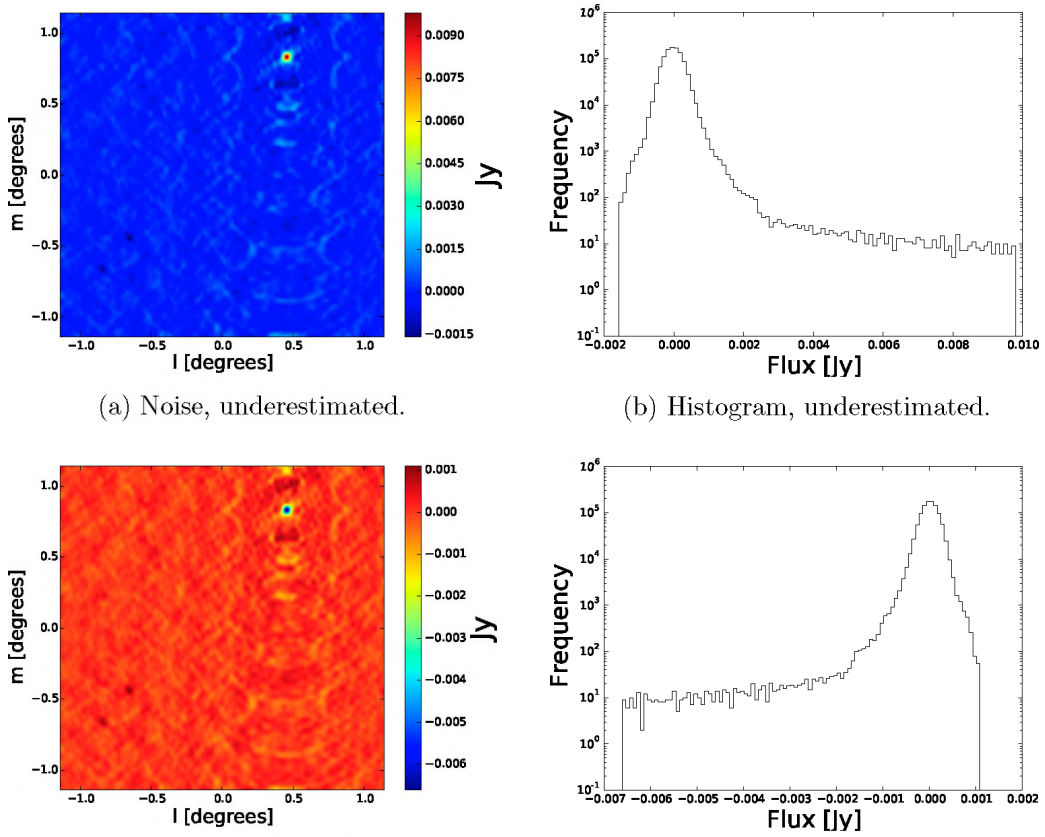

(a) Noise, underestimated.

(b) Histogram, underestimated.

(c) Noise, overestimated.

(d) Histogram, overestimated

FIGURE 3.12: Corrected residuals on the left and their histogram plots on the right showing the effects on the residuals' distribution. Top plots corresponds to simulations where the flux of the variable source is underestimated whereas in the bottom plots the flux of the variable source is overestimated.

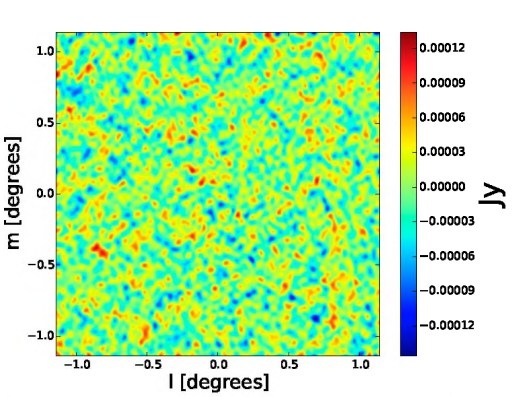

(a) Noise map when the variable source is correctly modelled.

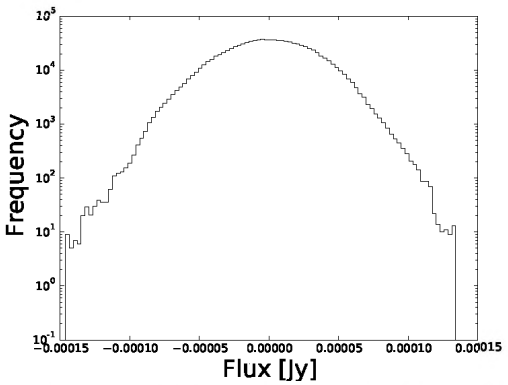

(b) Histogram plot of noise case when variable source is correctly modelled being almost perfectly symmetric.

FIGURE 3.13: Image of the corrected residuals when the variable source is properly modelled and its corresponding histogram. We can see from the histogram that when the all sources are modelled correctly, the residuals follow a perfect normal distribution.

Similarly as in the previous simulations we computed the ghost-subtracted residuals to minimize the effects of the secondary suppressor or secondary amplification ghost. The images are shown in Figure 3.14

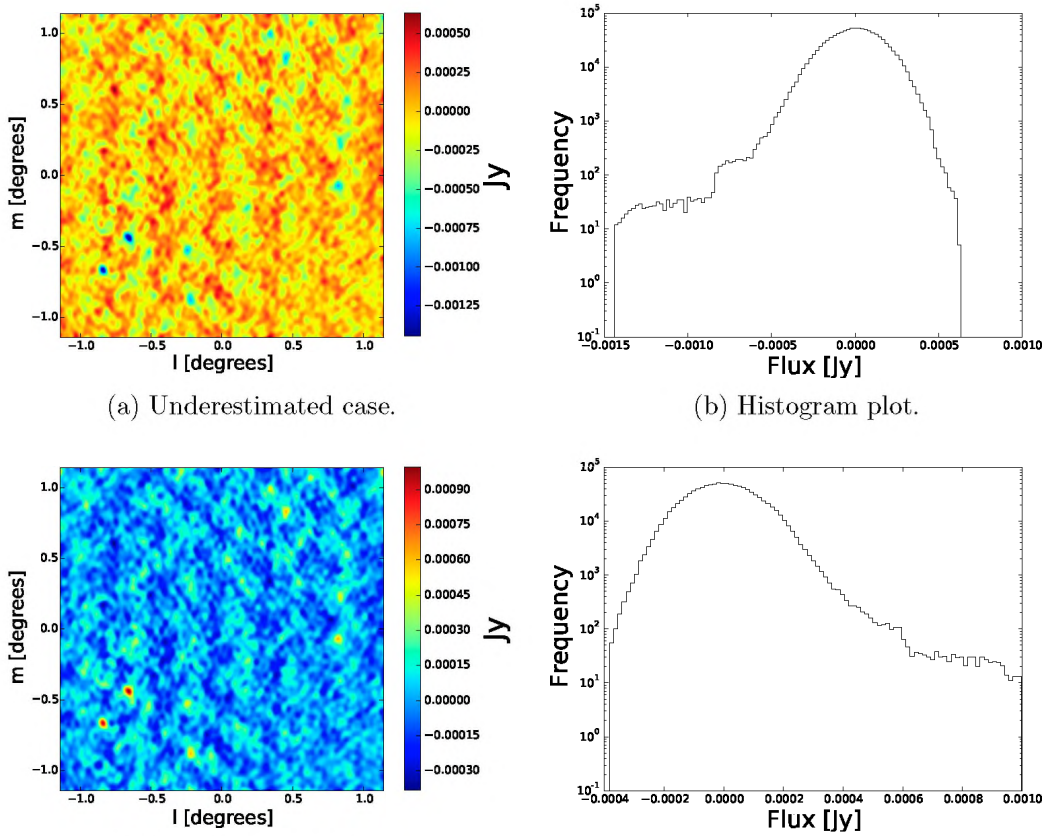

(a) Underestimated case.

(b) Histogram plot.

(c) Overestimated flux.

(d) Histogram plot.

FIGURE 3.14: Ghost-subtracted residuals on the left and histogram plots on the right showing the effects of the artefacts on the residuals' distribution.

Figure 3.15 shows plots in logarithm scales of rms of the residual images as they are stacked together.

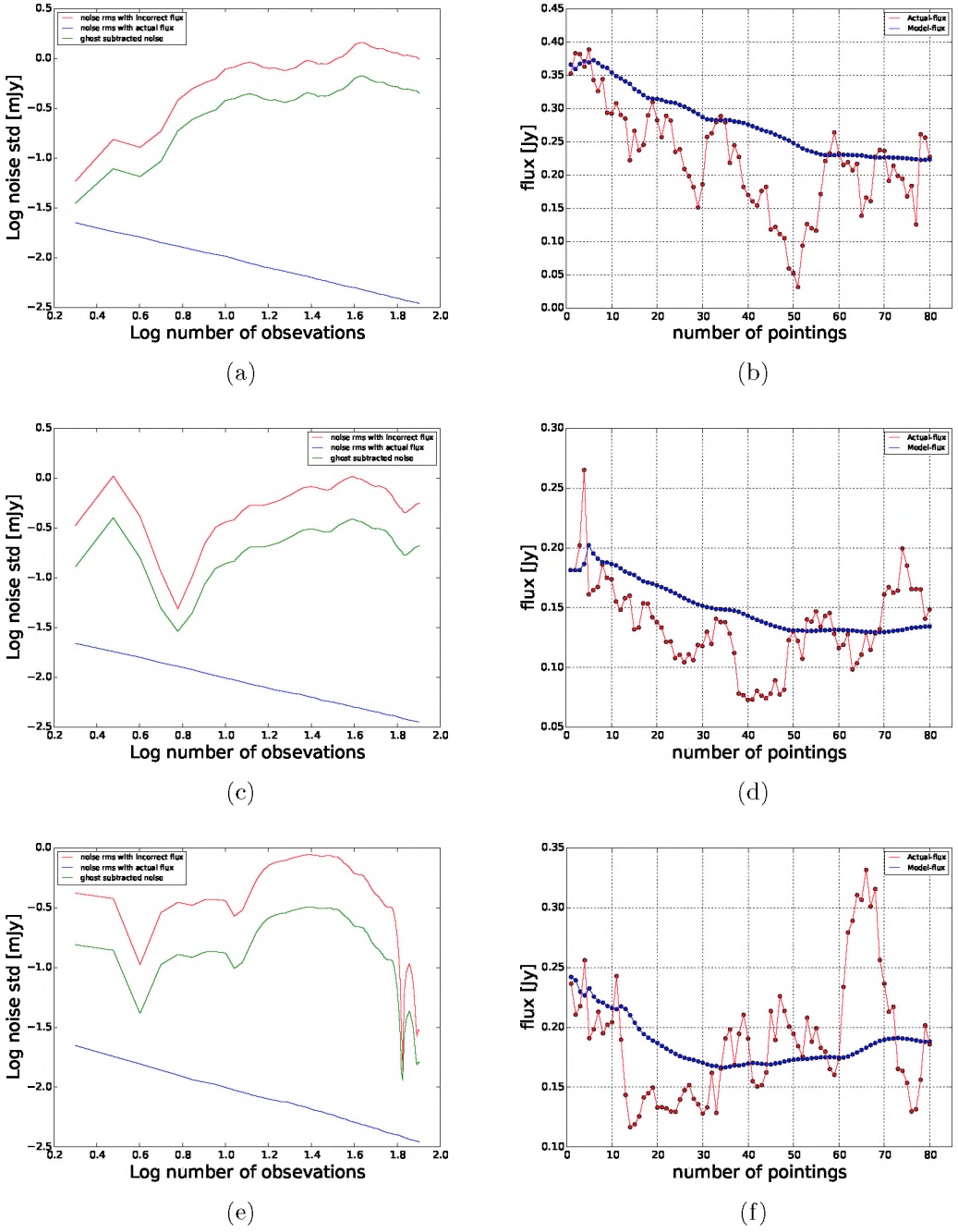

FIGURE 3.15: Left: Plots of log rms of the stacked images against the log of number images stacked together for eight experiments. The blue curve corresponds to the noise from simulations in which the correct sky model is used for calibration. The red curve corresponds to the noise from the corrected residuals when an incomplete sky model is used during calibration. The green curve corresponds to the noise from the ghost-subtracted residuals when the incomplete sky model is used during calibration. Right: Plot of the variable source light curve used for the simulation and the various flux values used to model the variable source during each calibration.

From the plots above we observe that the rms of the residual images do not average out as expected while the rms of the noise from the cases where the actual flux are

used during calibration do average out as expected. This is mainly because in the incorrectly modelled cases (both underestimated and overestimated), the artefacts have a large impact on the rms. Also, since the secondary suppressor always forms at the same position the averaged rms largely depends on the average value of the secondary suppressor ghost sources. Thus in cases where the sum total flux of the secondary suppressor ghost sources is approximately equal to that of the secondary amplification ghost sources, the final rms is very low. This is well illustrated with Figure 3.15e where we ended up with almost the same rms as the case where we used the actual flux during calibration. Also, as in the previous simulations, subtraction of the secondary suppressor ghost does not considerably reduce the rms level. The high rms again is attributed to all the other remaining artefacts which are not removed from the image and the residual flux from the secondary suppressor. This implies, in order to reduce these artefacts during calibration, we will need to perform several rounds of selfcal and carefully examine our residuals to have more information about what is missing in our sky models. We can not expect to always have variable sources, with normally distributed light curves which are modelled with their mean flux.

3.3.4.2 Fields with Multiple Variable Sources

The analysis for a field containing a single variable source presented in Section 3.3.4.1 can easily be extended to fields containing multiple variable sources. The contribution of each poorly modelled variable source is as explained in Section 3.2.1 and thus results in the presence of a very bright artefact in the noise map. This is illustrated in Figure 3.16.

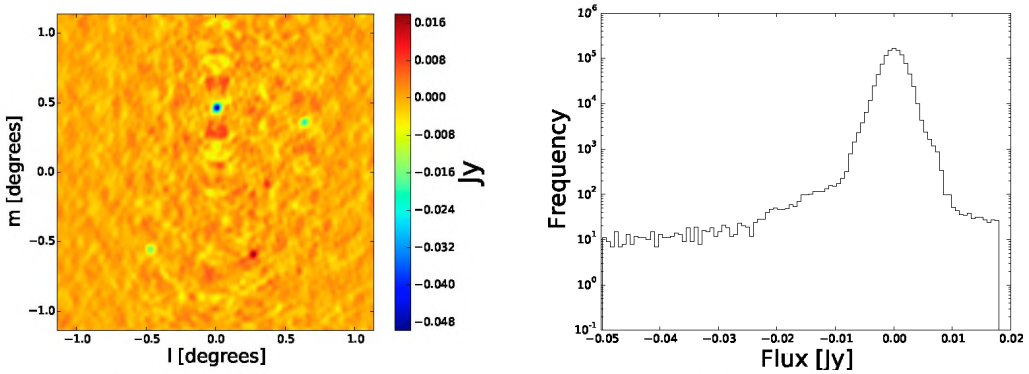

(a) 4 variable sources.

(b) Log histogram.

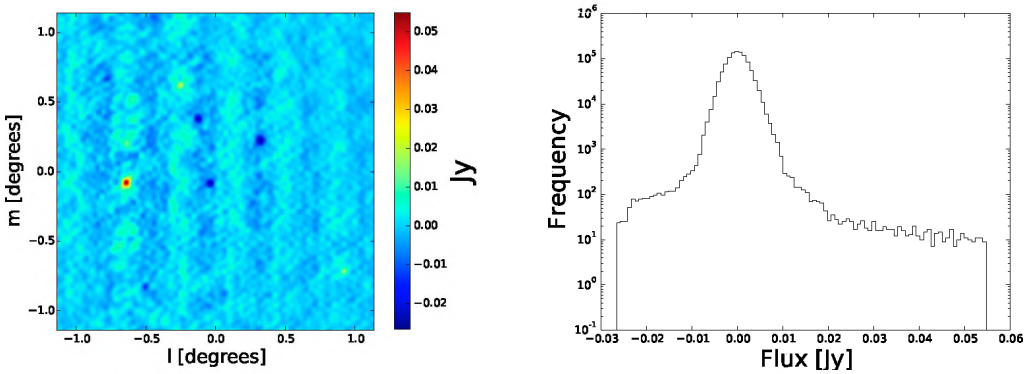

(c) 8 variable sources.

(d) Log histogram.

FIGURE 3.16: Noise and histogram plots for fields with 4 and 8 variable sources showing the presence of multiples bright artefacts in the noise map and non-normally distributed histograms.

The outputs for multiple variable sources are similar to that of a single variable source with the difference that the final image contains more bright artefacts as a result of the presence of multiple variable sources. Stacking in this case does not guarantee significant reductions in rms since the output residuals is not normally distributed.

NB. The presence of multiple bright artefacts makes it difficult to compute the ghost-subtracted residuals.

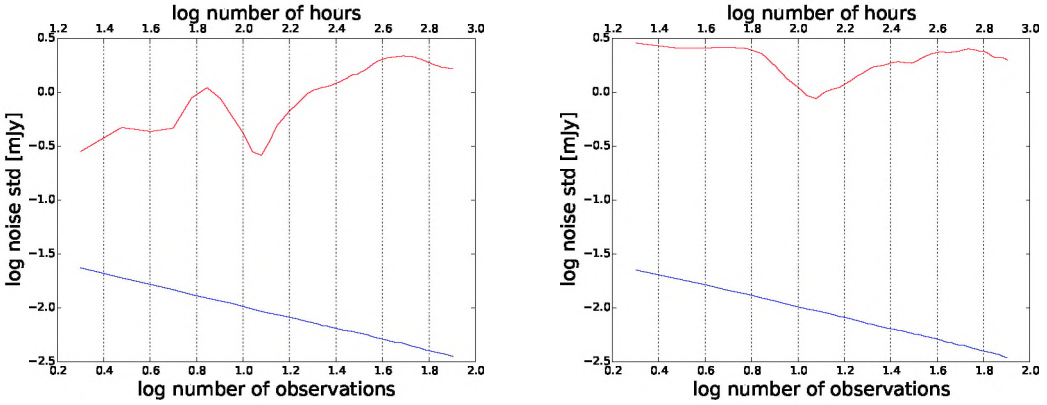

(a) 4 variable sources.

(b) 8 variable sources

FIGURE 3.17: Stacked log rms vs log number of observations for fields with multiple variable sources illustrating that the rms does not go down as expected.

3.4 Conclusions

From this study we highlight the following conclusions:

- The presence of variable sources leads to sky model errors whereby the flux of the variable sources are either overestimated or underestimated.
- We showed that both the underestimated and overestimated cases follow the same theory. The underestimated scenario resulted in the presence of a suppression ghost in the residual while the overestimated case led to the presence of an amplification ghost in the residuals. Both the suppression and amplification ghost were measured to be approximately $\frac{2}{N}\%$ of the unmodelled flux where N is the number of antennas in the interferometer.
- The presence of the variable source leads to residuals with very high rms. Furthermore we showed that even after the subtraction of the amplification or suppression ghost from the distilled residuals i.e. computing the ghost-subtracted residuals with Equation 3.6 did not significantly reduce the rms of the residuals.
- We also demonstrated that stacking the images together do not guarantee significant reduction in the rms of the residuals for a field containing variable sources. We showed that this was totally dependent on the skewness of the variable source's light curve with respect to the flux value used to modelled it. Future automatic calibration pipelines will have to implement an automatic selfcal. The automatic selfcal will enable to refine the sky models and correct for all sky model errors

such as incorrect fluxes for variable sources. This will be very important for future instruments such as MeerKAT and SKA which aim at unveiling the faintest emissions possible.

3.5 Summary

In this chapter, we studied the effects of long-term variable sources on the noise level in radio images. In the next chapter we extend the analysis by looking at the power spectrum of the residual visibilities.

Chapter 4

Power Spectrum Analysis

Epoch of Reionization (EoR) is the era in which matter in the intergalactic medium was ionised. Probing this era is one of the key science projects for SKA and most of the modern low frequency arrays such as LOFAR and PAPER. The EoR signal is very faint and detecting it requires subtraction or avoidance of foreground sources. However accurate foreground subtraction or avoidance will require almost perfect calibration of these new instruments. Recently a lot of work has been done to investigate how calibration artefacts will limit the detection of the EoR signal. This is done by studying the power spectrum of residuals obtained after inaccurate calibrations (Datta *et al.*, 2009, 2010; Barry *et al.*, 2016; Patil *et al.*, 2016; Ewall-Wice *et al.*, 2016).

Hence for completeness in this chapter we also estimate and compare the power spectrum from the *true residuals* and *ghost-subtracted residuals* obtained from our simulations in Chapter 3. We find that the power spectrum of both residuals is noise-like except that for the ghost-subtracted residuals is significantly higher. The rest of the chapter is divided as follows.

In Section 4.1 we describe our 1D power spectrum estimator using the simple example of a 1 Jy source located at the phase center. Next in Section 4.2 we compute and analyse the power spectrums from the true and ghost-subtracted residuals. Finally in Section 4.3 we draw conclusions from this analysis followed by a summary of the chapter in Section 4.4.

4.1 Power Spectrum Estimator

In Chapter 3, we only simulated single channel observations, thus we only construct a 1D power spectrum for the analysis. In basic terms, the power spectrum is defined as

the power, i.e. the absolute value square of the visibilities, per uv-distance (measured in units of wavelengths). Various methods such as the Fourier transform and the Maximum likelihood (Palanque-Delabrouille *et al.*, 2013) exist for computing 1D power spectrums. Here we implement a simple power spectrum estimator which computes the power spectrum directly from the visibilities by binning them radially and then averaging per bin.

Our estimator can be described using Equation 4.1 (Datta *et al.*, 2010).

$$P(k) = \frac{\sum_{|\boldsymbol{k}|=k} W(\boldsymbol{k})|V(\boldsymbol{k})|^2}{\sum_{|\boldsymbol{k}|=k} W(\boldsymbol{k})} \tag{4.1}$$

where $P(k)$ is the power spectrum per radial uv-distance, k, $V(\boldsymbol{k})$ is our visibilities, $W(\boldsymbol{k})$ represents the number of visibilities in the bin corresponding to k and $\boldsymbol{k} = (u, v)$ represents the (u, v) coordinates in vector form.

4.1.1 Gridding

The first step in estimating the power spectrum is to grid the visibilities on a uv-plane. Here the approach we employed is similar to natural weighting during imaging where each uv point's contribution is the sum of all the values that fall at that point. For KAT-7 the uv-points are roughly between -180 m to 180 m . We gridded our visibilities by redistributing the uv points on a 2D grid of cells with size 10 m using a nearest neighbour gridding kernel. For all the visibilities which fall in the same cell, their squared-sum is computed and then averaged. Figure 4.1 shows our uv coverage before and after gridding. We set all visibilities to 1 Jy. This corresponds to the visibilities of a 1 Jy source located at the phase center. Thus every point in the gridded plane with a measurement is red and all the points without any measurement are blue which corresponds to zero.

4.1.2 Binning and Averaging

The next step after gridding was to radially bin and average the visibilities. We used bins of radius equal to 3 cell sizes. Figure 4.2a shows the circular bins which were used. Figure 4.2b shows the resulting power spectrum obtained from the gridded and binned visibilities.

As expected it is a constant straight line whose value is 1 at all points. The y-axis values have been left in units of Jansky. We did not convert to millikelvins because our main goal was to measure the difference level between the power in the true and ghost-subtracted residuals. The x-axis values are in units of per degrees computed by

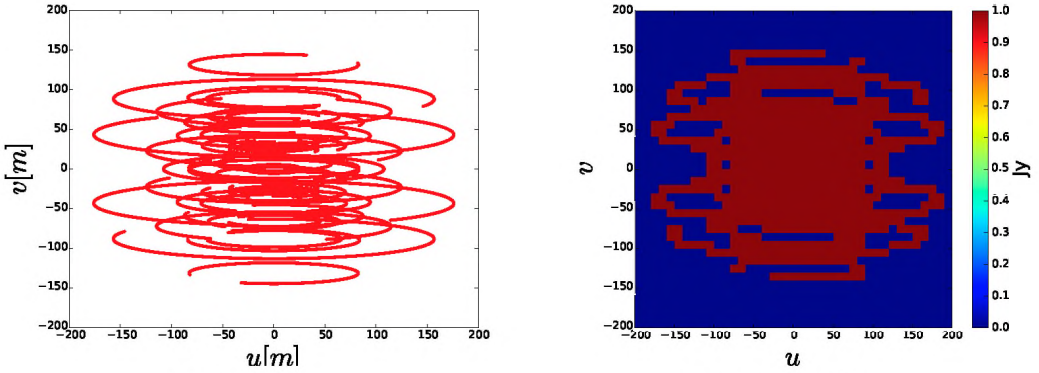

(a) UV coverage. (b) Gridded UV coverage.

FIGURE 4.1: Left: KAT-7 uv coverage at declination $\alpha = 15^h12^m50.5^s$ and right ascension $\delta = -09^d06^m00^s$ for 12 hours observation. Right: Gridded uv coverage

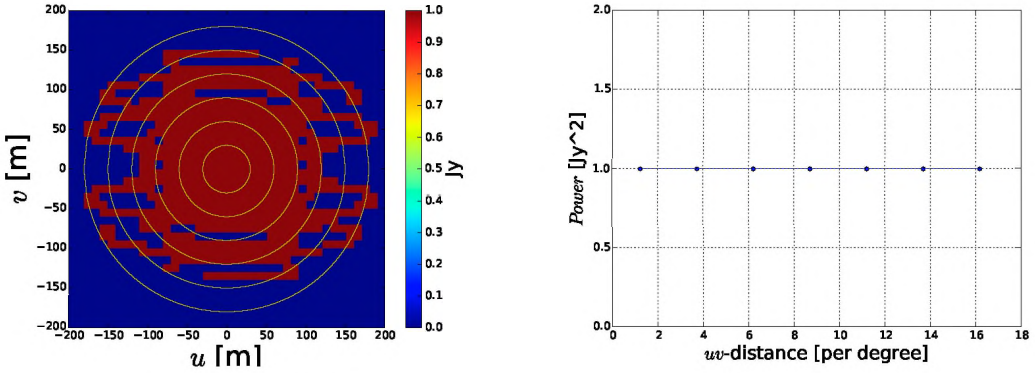

(a) Binned coverage (b) Power spectrum

FIGURE 4.2: Binned uv coverage and power spectrum obtained for a 1 Jy source located at the center of the field. The power spectrum is constant and equal to 1 as expected.

first scaling the uv-distances to per radians by dividing them with the corresponding wavelength (0.16 m) of the simulation and then converting from per radians to per degrees. All the pixels with no measurements (zero values) were removed from the bins before averaging.

This power spectrum estimator does not incorporate the w-term. This may influence the output given that KAT-7 is not an East-West array. However we do not expect this to significantly affect our results since we are dealing with a small field of view.

4.2 Results

We applied the power spectrum estimator to the residual obtained from the simulations in Chapter 3. Figure 4.3 shows the images of the residuals visibilities we used (Chapter 3 Figure 3.7a and 3.8c). In this simulation the flux of the variable source was overestimated

during calibration. The actual flux was 0.14 Jy and the model flux was 0.2 Jy, thus an excess flux of 0.06 Jy.

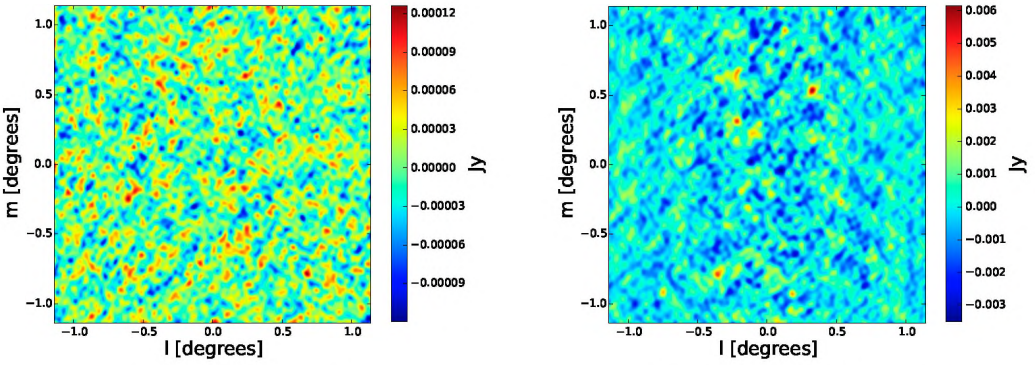

(a) True residuals.

(b) Ghost-subtracted residuals.

FIGURE 4.3: Images of the residual visibilities from which we computed the power spectrum. These images are duplicates of those shown in Chapter 3. They correspond to images of the true residuals and the ghost-subtracted residuals for one of the simulations.

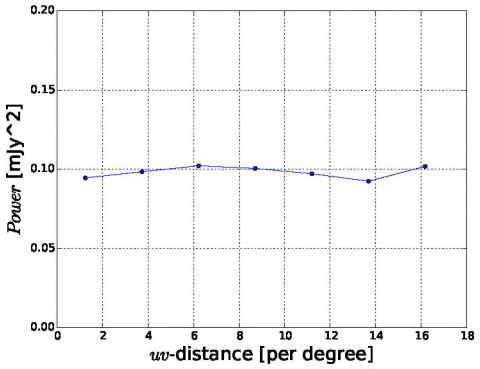

(a) True residuals

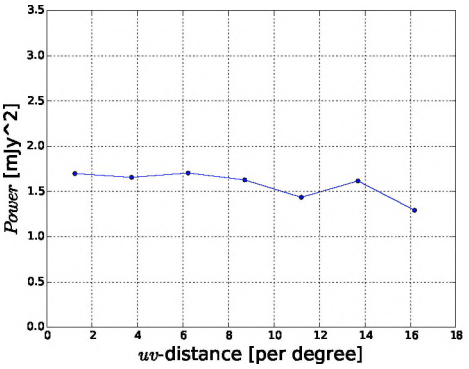

(b) Ghost-subtracted residuals.

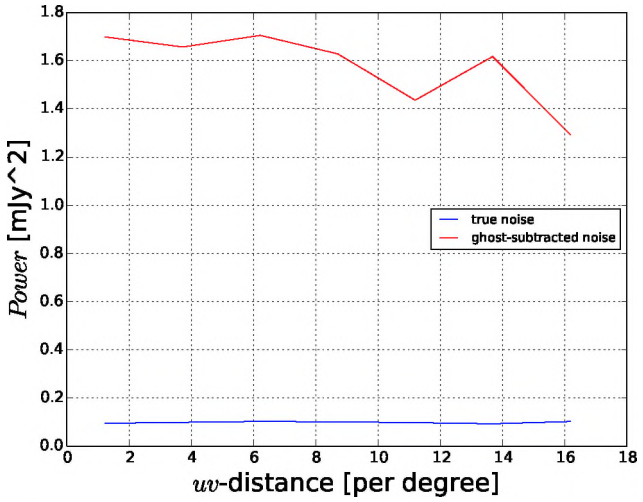

(c) Power spectrum for the ghost-subtracted and true residuals plot on the same figure. Here we can see the large difference in the power between the true residuals and the ghost-subtracted residuals.

FIGURE 4.4: Power Spectrum plots

Figure 4.4c shows the power spectrum we measured from the residuals. The individual power spectrum shown in Figure 4.4a and Figure 4.4b are both relatively constant. This is what we expect from the power spectrum of pure noise. Thus even the power spectrum from the ghost-subtracted residuals is noise-like. However our limited uv-coverage makes it difficult for us to identify if the ghost-subtracted residuals power spectrum has more power at specific scales. In Figure 4.4c both spectrum are plotted in the same figure. We can see the large difference in power between the ghost-subtracted residuals and the true residuals. This is as expected as we measured higher rms values for the ghost-subtracted residuals compared to the true residuals from our results in Chapter 3.

4.3 Conclusions

The following are the main conclusions we can draw from the above study.

- Both the true residuals and the ghost-subtracted residuals have almost flat power spectrums which is expected from noise-like residuals. The limited *uv*-coverage and the fact that we do not incorporate the w-term makes it difficult to determine if they have more power at specific scales from the ghost-subtracted residuals power spectrum.
- The ghost-subtracted residuals power spectrum is significantly higher than that of the true residuals. This shows that inaccurate modelling of a single source during calibration injects a significant amount of errors in the residuals. Thus future calibration pipelines will need to implement advanced techniques such as selfcal to be able to detect faint signals such as the EoR.

4.4 Summary

In this chapter, we extended the analysis of our results from Chapter 3 by looking at the power spectrum of our residual visibilities. The future EoR studies to be performed by SKA and new instruments will require almost perfect calibration. Using a simple and naive power spectrum estimator, we showed the large difference in power between residuals with artefacts and residuals without artefacts. In the next chapter we turn our attention to short-term variable sources.

Chapter 5

Calibration Artefacts from short-term Variable Sources

In the previous two chapter, we studied the effects of long-term variable sources on the root mean square (rms) of images after calibration. In this chapter we focus on short-term variable sources i.e. sources which vary on short time scales such as seconds, minutes and hours. Thus, such sources will vary within the time frame of an observation.

Variable sources are generally classified into two categories namely, intrinsic and extrinsic variable sources depending on the causes of the variability. Intrinsic variable sources are sources whose variability results from physical processes occurring within the radiating region of the source. Whereas extrinsic variable sources are sources whose observed luminosity changes due to processes such as absorption and reflection by the propagating medium or any propagation effect which induces an apparent variability in the source.

In this chapter we use the example of the apparent variability induced in sources by the primary beam when it rotates during observations. We show that in addition to the ghost sources observed in Chapter 3, short-term variations in sources' fluxes introduces other artefacts in the residuals during calibration. These additional artefacts cause an increase in the rms of the residual visibilities and sets the rms limit which can be achieved if selfcal is performed and the bright ghost sources are removed.

In Section 5.1 we describe how we obtained the light curve we used to represent short-term variability. Next, in Section 5.2 we present the simulation of field containing a short-term variable source which is modeled with the mean flux of its light curve during calibration. In Section 5.3, we perform simulations of a field containing a short-term variable source which is modelled with flux values other than its mean flux during calibration. Finally the main conclusions and summary of the chapter are provided in Sections 5.4 and 5.5 respectively.

5.1 The Variability Model

We used a variability model obtained by studying the effects of the primary beam on sources located far from the phase center. The primary beam, also known as the antenna radiation pattern, refers to the antenna response to radiation from different directions. Figure 5.1 shows an image of JVLA's (Jansky Very Large Array) primary beam at a frequency of 1.45 GHz.

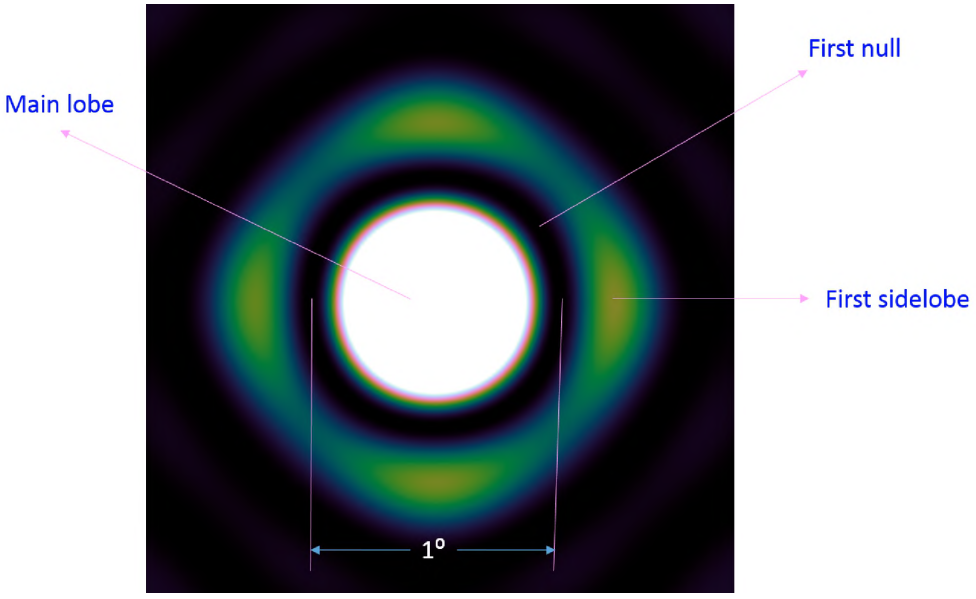

FIGURE 5.1: JVLA primary beam at 1.4 GHz.

Sources in the main lobe have the maximum gains while sources in the side lobes have the minimum gains and thus their fluxes are the most attenuated. Primary beam correction refers to applying the inverse beam gains in order to recover the true fluxes of the sources before attenuation by the primary beam. However during the course of an observation, the Earth rotates and sources occupy different positions in the sky. They are therefore attenuated by different beam gains and this results in the sources being extrinsically variable. Figure 5.2 shows an example of sources occupying different positions because of the Earth's rotation.

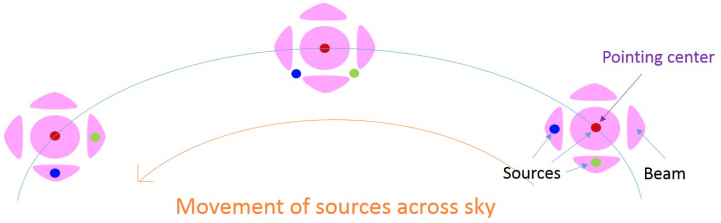

FIGURE 5.2: Sources occupying different positions and thus suffering different beam gains as result of Earth's rotation.

For this experiment, we interpolated the gains that a source located at a distance of 50 arcminutes from the phase center will be subject to over a 12 hour observation. We used the JVLA beam. Thus the variability model here is actually that of JVLA and not KAT-7, but this does not change the point we want to demonstrate with this experiment. Figure 5.3 shows the resulting light curve. Note that a lot of work such as Mitra *et al.* (2015) has been done on how to solve for the primary beam effects during calibration. We only use the primary beam induced variability as a representative example of short-term variability.

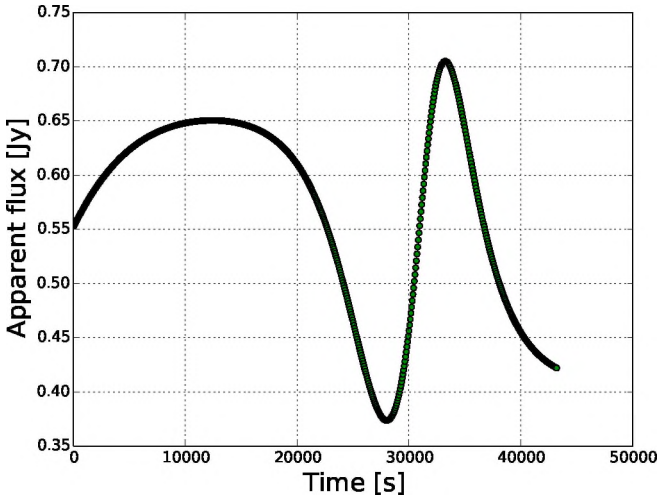

FIGURE 5.3: Light curve of a source with an intrinsic flux of 15 Jy, located 50 arcminutes from the phase center as result of attenuation by the JVLA primary beam at 1.45 GHz.

5.2 Variable Source Modelled with its Mean Flux

In this experiment, we performed a simulation of a field containing a variable source with the light curve in Figure 5.3. We used the pipeline and the same observation parameters described in Section 3.1 for the long-term simulations with the following modification.

- We manually compute the simulated visibilities as follows.

$$\boldsymbol{V}_{sim} = \sum_{s} I_s(t) e^{-2\pi i[ul+vm+w(\sqrt{1-l^2-m^2}-1)]} \tag{5.1}$$

where $\boldsymbol{V}_{sim}$ are the simulated visibilities, $I_s(t)$ represents the light curve of the source s, (u, v, w) are the antenna baseline coordinates or uv-coverage and (l, m) represents the sources' positions in the sky. For the non variable sources $I_s(t)$ is constant and

is equal to the source's flux density. For the variable source $I_s(t)$ is the light curve shown in Figure 5.3. The source was assume to vary over each observation timeslot or integration time of 60 s.

During calibration, all the non variable sources are modelled correctly with their respective flux densities and the variable source is modelled with its mean flux. The gains are computed per timeslots (60 s each) using the StEFCal algorithm. We also performed a parallel simulation without the variable source for comparison. After calibration we computed and imaged the corrected residuals as in Chapter 3.

$$\boldsymbol{V}_{res}^{corr} = \boldsymbol{G}^{-1}\boldsymbol{R}\boldsymbol{G}^{-H} - \boldsymbol{M} \tag{5.2}$$

where $\boldsymbol{V}_{res}^{corr}$ represents the corrected residuals, $\boldsymbol{R}$ the true visibilities, $\boldsymbol{M}$ the modelled visibilities and $\boldsymbol{G}$ the antenna gains. The plots in Figure 5.4 show the corrected residuals for the simulation of the field containing the variable source and that without the variable source.

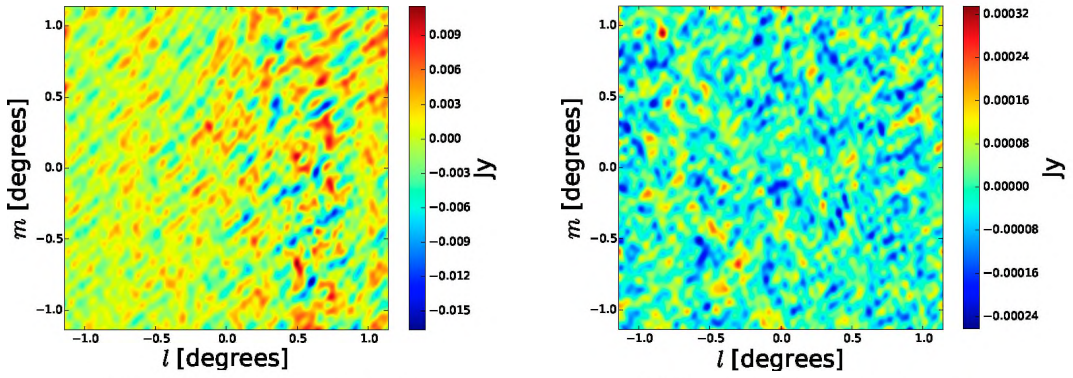

(a) Variable source present (b) No variable source present

FIGURE 5.4: Left: Corrected residuals for the field with the variable source. Right: Corrected residuals for the field without the variable source.

We observe from Figure 5.4 that, unlike the residuals from the simulations without the variable sources, those with the variable source have a lot of artefacts at a certain region in the image. This is the region surrounding the variable source. These result from the presence of the variable source which is approximated to its mean flux during imaging but the effects of the short variations in its flux are not removed. We verified this by simulating and imaging the visibilities of a source following the same light curve but having a mean of zero. As we can see from Figure 5.5 we obtained similar residuals as those in Figure 5.4a. Hence the presence of short-term variable sources causes the presence of certain artefacts which can not be removed by modelling the variable source flux with its mean flux during calibration.

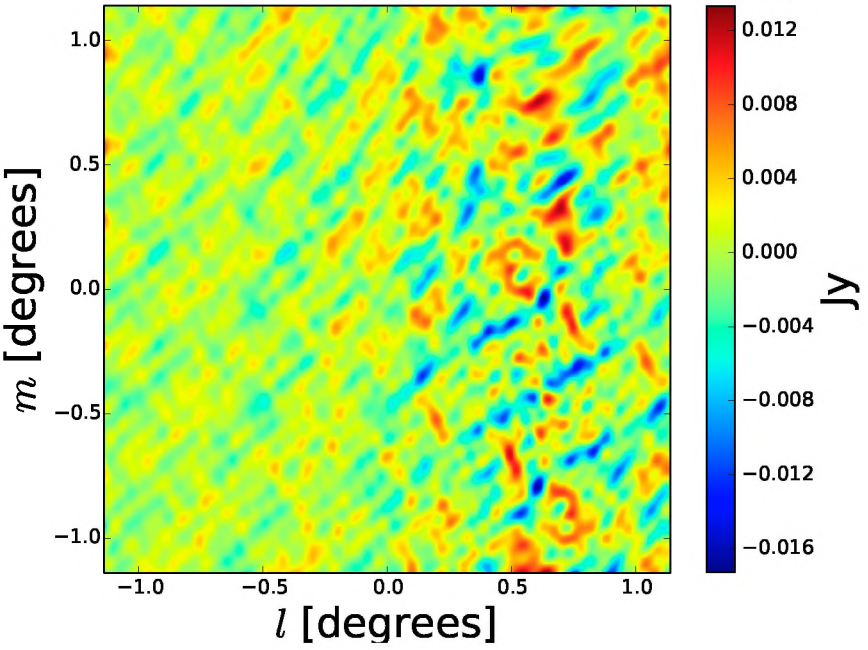

FIGURE 5.5: Imaged visibilities of variable source with light curve as shown in Figure 5.3 which has been normalised to mean zero.

5.3 Normal and Skew Simulations

In this section we repeat the simulations of Section 3.2 where the variable source light curve is either normal or skew distributed with respect to the flux value used to model it during calibration. Figure 5.6 is a plot of the probability density function of the variable source light curve in Figure 5.3. Here we performed several simulations where the variable source was modelled by each of the flux values indicated by the dotted lines in Figure 5.6. Thus the skewness of the variable with respect to its model flux changes with the simulations as the model flux changes. We define skewness similarly as in Section 3.2 using Equation 3.11.

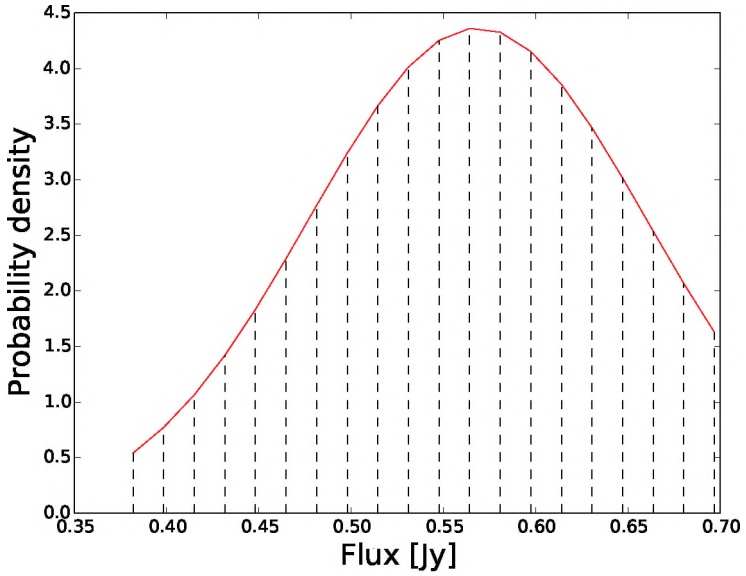

FIGURE 5.6: Probability density function of the variable source light curve. The red dotted line is the approximate probability density function of the variable source light curve and the black dotted lines are the different flux values used to modelled it in the different calibrations.

The plots in Figure 5.7 show two of the residual images obtained from the simulations. These results are similar to those from Section 3.2.1 with the underestimated and overestimated cases. The main difference is that in addition to the amplification or suppression ghost which arises from the flux of the variable source being underestimated or overestimated, we also have the artefacts described in Section 5.2, which result from the short-term variations from the mean flux of the variable source's flux.
NB. Overestimated and underestimated flux in this scenario means the model flux is greater than or less than the mean flux of the variable source respectively. Otherwise we can not define flux underestimation and overestimation here since the source is a short-term variable source and does not have a fixed flux during the simulated observation.

The plot in Figure 5.8 is a similar plot to that of the average ghost flux against the skewness of the variable source's light curve relative to the flux values used to model it during the different calibrations in Section 3.2.1. As in Chapter 3, we observed that for the ghost of the variable source to be totally eliminated we need to use a flux value close enough to the true mean flux of the variable source in order to have a skewness close to zero.

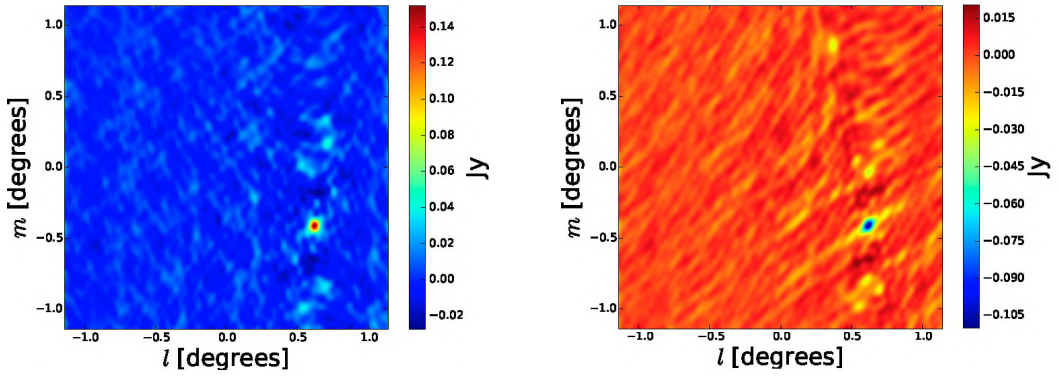

(a) (b)

FIGURE 5.7: Corrected residuals for simulations of a field containing a short-term variable source. On the left the variable source flux density is underestimated and on the right its flux density is overestimated.

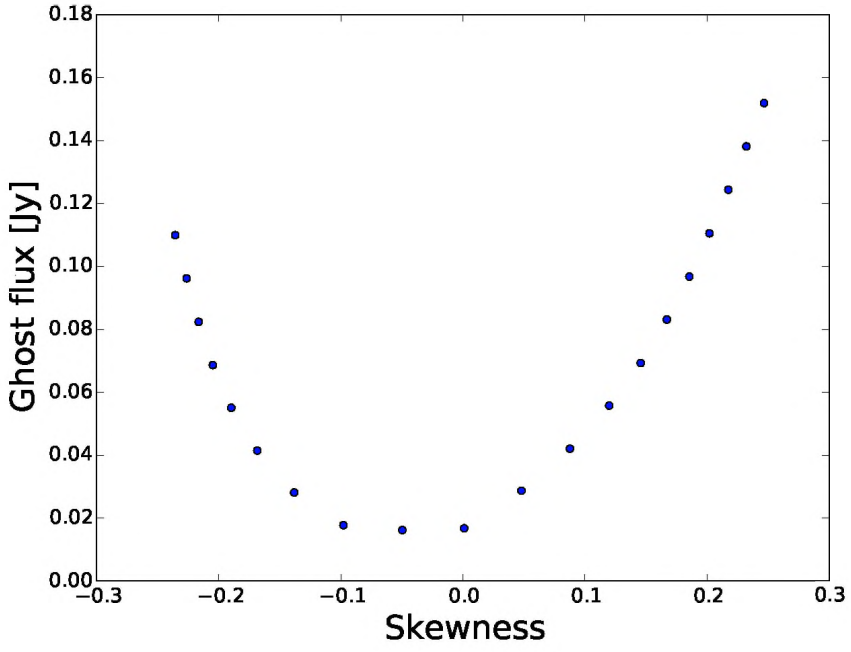

FIGURE 5.8: Brightest ghost flux against the skewness of the variable source's light curve relative to the flux values used during the different calibrations.

Figure 5.9 shows a plot of the rms computed using Equation 3.12 against the skewness for the various simulations before and after the subtraction of the amplification or suppression ghost. We observe that even after the subtraction of the amplification or suppression ghost the rms is still very high compared to that of a simulation with no variable source. This is because of the artefacts from the short-term variability, explained in Section 5.2 which can not be removed. Thus, in contrast to long-term variability

simulations of Section 3.2, even if a short-term variable source is modelled with its mean flux (zero skewness), no ghost artefact will be created but the residual rms will still be higher compared to thermal noise because of the short-term variability.

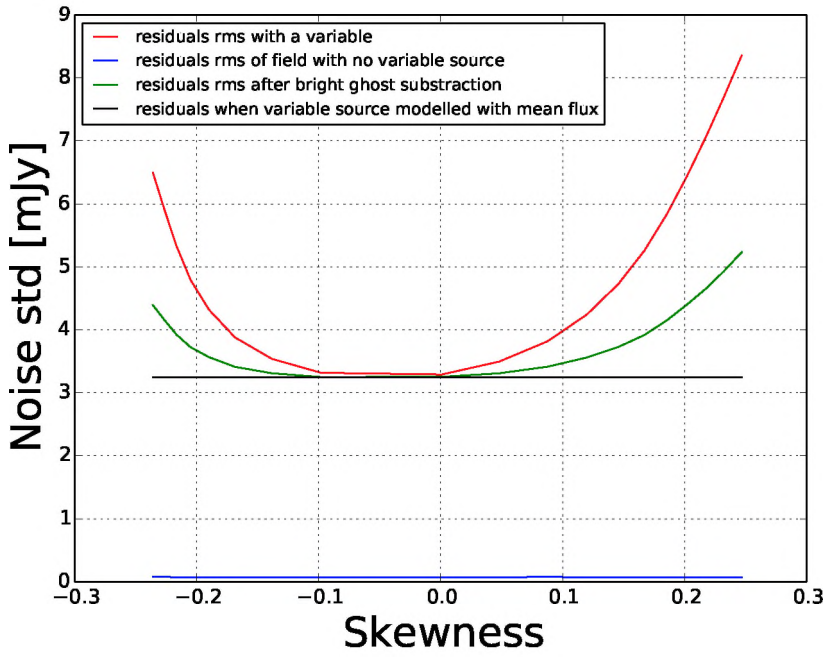

FIGURE 5.9: Rms of the residuals images against the skewness of the variable source light curve relative to the flux values used during the different calibrations.

From Figure 5.9 we also observe that the rms before the subtraction of the ghost depends on the skewness in the same way as the amplification or suppression ghost flux in Figure 5.8. This is because the ghost artefacts are much brighter than the short-term variability artefacts and thus have a higher contribution to the residual rms. After the subtraction of the ghost the rms should be constant and equal to that when the variable source is modelled with its mean flux. This rms is the limit which can be achieved, since the short-term artefacts can not be removed. This is not the case because the estimation and subtraction of the ghost flux is not perfect.

5.4 Conclusions

We draw the following two conclusions from these simulations:

- The presence of short-term variable sources leads to the introduction of new artefacts in the residuals. These artefacts can not be removed even when the variable source is modelled with its mean flux.

- When the short-term variable source is modeled with a flux lower than or greater than its mean flux, a suppressor or amplification ghost forms in addition to those from the short-term variability artefacts. The artefacts from the suppressor and amplification ghost are much brighter than those from the short-term variability, thus when present contributes the most to the residuals' rms.

5.5 Summary

In this chapter we extended the work of Chapter 3 to short-term variable sources. We briefly discussed the primary beam, which is the antenna radiation pattern and explained how it induces variability in sources as a result of the Earth's rotation. Using a variability model obtained from the primary beam we performed simulations of a field containing a short-term variable source and studied its effects on the residuals and the noise level. In the next chapter we present general conclusions from this thesis and future research works.

Chapter 6

Conclusion and Future Works

Conclusions

This thesis provides us with an understanding of the effects of ignoring variable sources during calibration. This thesis consists mainly of two sets of simulations. In the first set of simulations, we focussed on long-term variable sources and studied how they affect the rms of residual visibilities. These simulations are an extension to Grobler *et al.* (2014) and Wijnholds *et al.* (2016), with the difference that here we included thermal noise in our simulations, considered a field with more sources (30 instead of 2) and situations where the fluxes of sources are overestimated.

The results from the long term variable sources simulations showed that when a source flux is not modelled correctly, this introduces a bright ghost source at the position of the source in the residual visibilities. We observed that the overestimation and underestimation of a source's flux leads to similar results but the ghost sources fluxes have different signs. We defined an analogue to the secondary suppressor ghost from Wijnholds *et al.* (2016) which we called the secondary amplification ghost. The measured suppression rates agreed with Wijnholds *et al.* (2016) predictions.

The second step in the analysis of the long-term simulations was to compare the rms of residuals with the variable source to those with no variable source. We measured higher rms from the residuals with the variable source. Even the subtraction of the secondary suppressor and/or amplification ghost from the residuals did not considerably reduce its rms. Stacking of the residuals showed that the residuals from the simulations with the variable source were not normally distributed and their rms did not reduce as is expected when images are stacked together. We showed that for ghost sources to cancel out completely, the light curve of the variable sources had to have a skewness of 0 relative to the flux value used to model it during calibration.

The final step in the analysis of the residuals from the long-term simulations was to compute and compare the power spectrum of the residuals with the variable source to those with no variable source. As expected from the rms results, we measured a higher power in the residuals with the variable source compared to those without any variable source. The limited *uv*-coverage made it difficult to detect if there was more power at specific scales (high power at a certain scale implies the presence of a source at this scale) from the residuals with the variable source.

We also performed a second set of simulations to investigate the effects of short-term variable sources on residual visibilities. The output from these simulations showed that short-term variable sources introduces different kinds of artefacts into the residual visibilities. We showed that these artefacts were directly linked to the short variations in the flux of the short-term variable source. Similarly, as with the long-term variable source, these artefacts lead to an increase in the rms of the residual visibilities.

Future Works

- The first possible extension to this work will be to further investigate the effects of the short-term variable sources. This may be by calibrating and imaging the visibility data on a single time slot basis, then progressively combining the visibilities from different time slots and observing how the artefacts combine.
- A second extension will be to improve the power spectrum analysis of the long-term residuals by constructing a better power spectrum estimator which accounts for the w-term. This analysis can also be performed on the residuals from the short-term variability simulations.
- In order to get better knowledge of how variable sources will affect large arrays like MeerKAT, we will need to do extensive simulations with such arrays. These will have to be done using accurate beam models for these arrays, and considering larger fields with a more realistic population of sources.

Appendix A

Appendix A: Bending Power Law and Gamma Distribution Python Functions

```
def BendingPL(v,A,v_bend,a_low,a_high,c):
    '''
    Bending power law function - returns power at each value of v,
    where v is an array (e.g. of frequencies)

    inputs:
        v (array)       - input values
        A (float)       - normalisation
        v_bend (float)  - bending frequency
        a_low ((float)  - low frequency index
        a_high float)   - high frequency index
        c (float)       - intercept/offset
    output:
        out (array)     - output powers
    '''
    numer = v**-a_low
    denom = 1 + (v/v_bend)**(a_high-a_low)
    out = A * (numer/denom) + c
    return out

def RandAnyDist(f,args,a,b,size=1):
    '''
    Generate random numbers from any distribution. Slow.

    inputs:
        f (function f(x,**args)) - The distribution from which numbers are drawn
        args (tuple) - The arguments of f (excluding the x input array)
        a,b (float)  - The range of values for x
        size (int, optional) - The size of the resultant array of random values,
                               returns a single value as default
    outputs:
```

```
        out (array) - List of random values drawn from the input distribution
    '''
    out = []
    while len(out) < size:
        x = rnd.rand()*(b-a) + a  # random value in x range
        v = f(x,*args)            # equivalent probability
        p = rnd.rand()      # random number
        if p <= v:
            out.append(x)   # add to value sample if random number < probability
    if size == 1:
        return out[0]
    else:
        return out
```

Bibliography

Md Faijul Amin, Muhammad Ilias Amin, Ahmed Yarub H Al-Nuaimi, and Kazuyuki Murase. Wirtinger calculus based gradient descent and levenberg-marquardt learning algorithms in complex-valued neural networks. In *International Conference on Neural Information Processing*, pages 550–559. Springer, 2011.

Anna Barnacka, Rafal Moderski, Bagmeet Behera, Pierre Brun, and Stefan Wagner. PKS 1510-089: a rare example of a flat spectrum radio quasar with a very high-energy emission. *Astronomy & Astrophysics*, 567:A113, 2014.

N Barry, B Hazelton, I Sullivan, MF Morales, and JC Pober. Calibration requirements for detecting the 21 cm epoch of reionization power spectrum and implications for the ska. *Monthly Notices of the Royal Astronomical Society*, page stw1380, 2016.

S Bhatnagar, TJ Cornwell, K Golap, and Socorro NRAO. Evla memo 84. solving for the antenna based pointing errors. Technical report, Tech. rep., NRAO, 2004.

S Bhatnagar, TJ Cornwell, K Golap, and Juan M Uson. Correcting direction-dependent gains in the deconvolution of radio interferometric images. *Astronomy & Astrophysics*, 487(1):419–429, 2008.

AJ Boonstra and AJ Van Der Veen. Gain decomposition methods for radio telescope arrays. In *Statistical Signal Processing, 2001. Proceedings of the 11th IEEE Signal Processing Workshop on*, pages 365–368. IEEE, 2001.

RS Booth, WJG De Blok, JL Jonas, and B Fanaroff. Meerkat key project science, specifications, and proposals. *arXiv preprint arXiv:0910.2935*, 2009.

Max Born and Emil Wolf. Principles of optics electromagnetic theory of propagation. *Principles of Optics Electromagnetic Theory of Propagation, INterference and Diffraction of Light 2nd edition by Max Born, Emil Wolf New York, NY: Pergamon Press, 1964*, 1, 1964.

Samuel D Connolly. Delightcurvesimulation: Light curve simulation code. *Astrophysics Source Code Library*, 2016.

Tim Cornwell, Robert Braun, and Daniel S Briggs. Deconvolution. In *Synthesis Imaging in Radio Astronomy II*, volume 180, page 151, 1999.

TJ Cornwell and PN Wilkinson. A new method for making maps with unstable radio interferometers. *Monthly Notices of the Royal Astronomical Society*, 196(4):1067–1086, 1981.

A Datta, S Bhatnagar, and CL Carilli. Detection of signals from cosmic reionization using radio interferometric signal processing. *The Astrophysical Journal*, 703(2):1851, 2009.

A Datta, JD Bowman, and CL Carilli. Bright source subtraction requirements for redshifted 21 cm measurements. *The Astrophysical Journal*, 724(1):526, 2010.

Ronald D Ekers. The almost serendipitous discovery of self-calibration. In *Serendipitous Discoveries in Radio Astronomy*, volume 1, page 154, 1984.

D Emmanoulopoulos, IM McHardy, and IE Papadakis. Generating artificial light curves: revisited and updated. *Monthly Notices of the Royal Astronomical Society*, 433(2): 907–927, 2013.

Aaron Ewall-Wice, Joshua S Dillon, Adrian Liu, and Jacqueline Hewitt. The impact of modeling errors on interferometer calibration for 21 cm power spectra. *arXiv preprint arXiv:1610.02689*, 2016.

Rob Fender, A Stewart, JP Macquart, *et al.* The transient universe with the square kilometre array. *proceedings of "Advancing Astrophysics with the Square Kilometre Array", PoS (AASKA14)*, 51, 2015.

RS Foster, EB Waltman, M Tavani, BA Harmon, SN Zhang, WS Paciesas, and FD Ghigo. Radio and x-ray variability of the galactic superluminal source grs 1915+ 105. *The Astrophysical Journal Letters*, 467(2):L81, 1996.

TL Grobler, CD Nunhokee, OM Smirnov, AJ Van Zyl, and AG De Bruyn. Calibration artefacts in radio interferometry–i. ghost sources in westerbork synthesis radio telescope data. *Monthly Notices of the Royal Astronomical Society*, 439(4):4030–4047, 2014.

TL Grobler, AJ Stewart, SJ Wijnholds, JS Kenyon, and OM Smirnov. Calibration artefacts in radio interferometry–iii. phase-only calibration and primary beam correction. *Monthly Notices of the Royal Astronomical Society*, 461(3):2975–2992, 2016.

JP Hamaker, JD Bregman, and RJ Sault. Understanding radio polarimetry. i. mathematical foundations. *Astronomy and Astrophysics Supplement Series*, 117(1):137–147, 1996.

DS Heeschen, Th Krichbaum, CJ Schalinski, and A Witzel. Rapid variability of extragalactic radio sources. *The Astronomical Journal*, 94:1493–1507, 1987.

JA Högbom. Aperture synthesis with a non-regular distribution of interferometer baselines. *Astronomy and Astrophysics Supplement Series*, 15:417, 1974.

Karl G Jansky. Electrical disturbances apparently of extraterrestrial origin. *Proceedings of the Institute of Radio Engineers*, 21(10):1387–1398, 1933.

RC Jennison. A phase sensitive interferometer technique for the measurement of the fourier transforms of spatial brightness distributions of small angular extent. *Monthly Notices of the Royal Astronomical Society*, 118(3):276–284, 1958.

Akiko Kadota, Kenta Fujisawa, Satoko Sawada-Satoh, Kiyoaki Wajima, and Akihiro Doi. An intrinsic short-term radio variability observed in PKS 1510- 089. *Publications of the Astronomical Society of Japan*, 64(5):109, 2012.

S Kazemi and S Yatawatta. Robust radio interferometric calibration using the t-distribution. *Monthly Notices of the Royal Astronomical Society*, 435(1):597–605, 2013.

S Kazemi, S Yatawatta, S Zaroubi, P Lampropoulos, AG de Bruyn, LVE Koopmans, and J Noordam. Radio interferometric calibration using the sage algorithm. *Monthly Notices of the Royal Astronomical Society*, 414(2):1656–1666, 2011.

KI Kellermann and IIK Pauliny-Toth. Variable radio sources. *Annual Review of Astronomy and Astrophysics*, 6:417, 1968.

John D Kraus. Radio astronomy. *New York: McGraw-Hill, 1966*, 1, 1966.

Kenneth Levenberg. A method for the solution of certain non–linear problems in least squares. 1944.

Lukas Lindroos, KK Knudsen, W Vlemmings, J Conway, and I Martí-Vidal. Stacking of large interferometric data sets in the image-and uv-domain–a comparative study. *Monthly Notices of the Royal Astronomical Society*, 446(4):3502–3515, 2015.

RP Linfield. A modified hybrid mapping technique for vlbi data. *The Astronomical Journal*, 92:213–218, 1986.

Kaj Madsen, Hans Bruun Nielsen, and Ole Tingleff. Methods for non-linear least squares problems. 2004.

Donald W Marquardt. An algorithm for least-squares estimation of nonlinear parameters. *Journal of the society for Industrial and Applied Mathematics*, 11(2):431–441, 1963.

Iván Martí-Vidal and JM Marcaide. Spurious source generation in mapping from noisy phase-self-calibrated data. *Astronomy & Astrophysics*, 480(1):289–295, 2008.

Daniel A Mitchell, Lincoln J Greenhill, Randall B Wayth, Robert J Sault, Colin J Lonsdale, Roger J Cappallo, Miguel F Morales, and Stephen M Ord. Real-time calibration of the murchison widefield array. *IEEE Journal of Selected Topics in Signal Processing*, 2(5):707–717, 2008.

Modhurita Mitra, Sphesihle Makhathini, Griffin Foster, Oleg Smirnov, and Richard Perley. Incorporation of antenna primary beam patterns in radio-interferometric data reduction to produce wide-field, high-dynamic-range images. In *Electromagnetics in Advanced Applications (ICEAA), 2015 International Conference on*, pages 494–497. IEEE, 2015.

KP Mooley, G Hallinan, S Bourke, A Horesh, ST Myers, DA Frail, SR Kulkarni, DB Levitan, MM Kasliwal, SB Cenko, *et al.* The caltech-nrao stripe 82 survey (cnss) paper. i. the pilot radio transient survey in 50 deg2. *The Astrophysical Journal*, 818(2):105, 2016.

Jan E Noordam. Lofar calibration challenges. In *SPIE Astronomical Telescopes+ Instrumentation*, pages 817–825. International Society for Optics and Photonics, 2004.

Jan E Noordam and Oleg M Smirnov. The meqtrees software system and its use for third-generation calibration of radio interferometers. *Astronomy & Astrophysics*, 524: A61, 2010.

Chuneeta Devi Nunhokee. Link between ghost artefacts, source suppression and incomplete calibration sky models. *MSc thesis, Rhodes University*, 2015.

A. R. Offringa, J. J. van de Gronde, and J. B. T. M. Roerdink. A morphological algorithm for improved radio-frequency interference detection. *A&A*, 539, March 2012.

N Oozeer, T Mauch, and R Booth. Blazar monitoring with KAT-7: PKS 1510-089 a test case. *Memorie della Societa Astronomica Italiana*, 86:42, 2015.

Rachel A Osten and TS Bastian. Ultrahigh time resolution observations of radio bursts on ad leonis. *The Astrophysical Journal*, 674(2):1078, 2008.

Nathalie Palanque-Delabrouille, Christophe Yèche, Arnaud Borde, Jean-Marc Le Goff, Graziano Rossi, Matteo Viel, Éric Aubourg, Stephen Bailey, Julian Bautista, Michael Blomqvist, *et al.* The one-dimensional lyα forest power spectrum from boss. *Astronomy & Astrophysics*, 559:A85, 2013.

Ajinkya H Patil, Sarod Yatawatta, Saleem Zaroubi, Léon VE Koopmans, AG de Bruyn, Vibor Jelić, Benedetta Ciardi, Ilian T Iliev, Maaijke Mevius, Vishambhar N Pandey, *et al.* Systematic biases in low-frequency radio interferometric data due to calibration: the lofar-eor case. *Monthly Notices of the Royal Astronomical Society*, 463(4):4317–4330, 2016.

RA Perley, CJ Chandler, BJ Butler, and JM Wrobel. The expanded very large array: a new telescope for new science. *The Astrophysical Journal Letters*, 739(1):L1, 2011.

ACS Readhead and PN Wilkinson. The mapping of compact radio sources from vlbi data. *The Astrophysical Journal*, 223:25–36, 1978.

A Rowlinson, ME Bell, T Murphy, CM Trott, N Hurley-Walker, S Johnston, SJ Tingay, DL Kaplan, D Carbone, PJ Hancock, *et al.* Limits on fast radio bursts and other transient sources at 182 mhz using the murchison widefield array. *Monthly Notices of the Royal Astronomical Society*, 458(4):3506–3522, 2016.

Stef Salvini and Stefan J Wijnholds. Stefcal—an alternating direction implicit method for fast full polarization array calibration. In *General Assembly and Scientific Symposium (URSI GASS), 2014 XXXIth URSI*, pages 1–4. IEEE, 2014.

Richard T Schilizzi, Peter EF Dewdney, and T Joseph W Lazio. The square kilometre array. In *SPIE Astronomical Telescopes+ Instrumentation*, pages 70121I–70121I. International Society for Optics and Photonics, 2008.

O. M. Smirnov. Revisiting the radio interferometer measurement equation. III. Addressing direction-dependent effects in 21 cm WSRT observations of 3C 147. , 527:A108, March 2011. doi: 10.1051/0004-6361/201116435.

Oleg M Smirnov. Revisiting the radio interferometer measurement equation-i. a full-sky jones formalism. *Astronomy & Astrophysics*, 527:A106, 2011.

OM Smirnov and Cyril Tasse. Radio interferometric gain calibration as a complex optimization problem. *Monthly Notices of the Royal Astronomical Society*, 449(3): 2668–2684, 2015.

FG Smith. The measurement of the angular diameter of radio stars. *Proceedings of the Physical Society. Section B*, 65(12):971, 1952.

Laurent Sorber, Marc Van Barel, and Lieven De Lathauwer. Unconstrained optimization of real functions in complex variables. *SIAM Journal on Optimization*, 22(3):879–898, 2012.

AJ Stewart, RP Fender, JW Broderick, TE Hassall, T Muñoz-Darias, A Rowlinson, JD Swinbank, TD Staley, GJ Molenaar, B Scheers, *et al.* Lofar msss: detection of a low-frequency radio transient in 400 h of monitoring of the north celestial pole. *Monthly Notices of the Royal Astronomical Society*, 456(3):2321–2342, 2016.

Cyril Tasse. Nonlinear kalman filters for calibration in radio interferometry. *Astronomy & Astrophysics*, 566:A127, 2014.

A Richard Thompson, James M Moran, and George W Swenson Jr. *Interferometry and synthesis in radio astronomy.* John Wiley & Sons, 2008.

Nithyanandan Thyagarajan, David J Helfand, Richard L White, and Robert H Becker. Variable and transient radio sources in the first survey. *The Astrophysical Journal*, 742(1):49, 2011.

Marie-Helene Ulrich, Laura Maraschi, and C Megan Urry. Variability of active galactic nuclei. *Annual Review of Astronomy and Astrophysics*, 35(1):445–502, 1997.

MP Van Haarlem, MW Wise, AW Gunst, George Heald, JP McKean, JWT Hessels, AG De Bruyn, Ronald Nijboer, John Swinbank, Richard Fallows, *et al.* Lofar: The low-frequency array. *Astronomy & Astrophysics*, 556:A2, 2013.

SJ Wijnholds, TL Grobler, and OM Smirnov. Calibration artefacts in radio interferometry–ii. ghost patterns for irregular arrays. *Monthly Notices of the Royal Astronomical Society*, 457(3):2331–2354, 2016.

PN Wilkinson, J Conway, and J Biretta. Developments in continuum imaging. In *The Impact of VLBI on Astrophysics and Geophysics*, volume 129, pages 509–518, 1988.

Sarod Yatawatta. Radio interferometric calibration using a riemannian manifold. In *Acoustics, Speech and Signal Processing (ICASSP), 2013 IEEE International Conference on*, pages 3866–3870. IEEE, 2013.

Sarod Yatawatta, Sanaz Kazemi, and Saleem Zaroubi. Gpu accelerated nonlinear optimization in radio interferometric calibration. In *Innovative Parallel Computing (InPar), 2012*, pages 1–6. IEEE, 2012.